

This is an Open Access document downloaded from ORCA, Cardiff University's institutional repository:<https://orca.cardiff.ac.uk/id/eprint/131591/>

This is the author's version of a work that was submitted to / accepted for publication.

Citation for final published version:

Pudkon, Watcharapong, Bahruji, Hasliza, Miedziak, Peter J., Davies, Thomas E., Morgan, David J. , Pattison, Samuel, Kaowphong, Sulawan and Hutchings, Graham J. 2020. Enhanced visible-light-driven photocatalytic H<sub>2</sub> production and Cr(vi) reduction of a ZnIn<sub>2</sub>S<sub>4</sub>/MoS<sub>2</sub> heterojunction synthesized by the biomolecule-assisted microwave heating method. *Catalysis Science and Technology* 10 (9) , pp. 2838-2854. 10.1039/D0CY00234H

Publishers page: <http://dx.doi.org/10.1039/D0CY00234H>

Please note:

Changes made as a result of publishing processes such as copy-editing, formatting and page numbers may not be reflected in this version. For the definitive version of this publication, please refer to the published source. You are advised to consult the publisher's version if you wish to cite this paper.

This version is being made available in accordance with publisher policies. See <http://orca.cf.ac.uk/policies.html> for usage policies. Copyright and moral rights for publications made available in ORCA are retained by the copyright holders.



**Enhanced visible-light-driven photocatalytic H<sub>2</sub> production and Cr(VI) reduction of a ZnIn<sub>2</sub>S<sub>4</sub>/MoS<sub>2</sub> heterojunction synthesized by the biomolecule-assisted microwave heating method**

Watcharapong Pudkon<sup>a</sup>, Hasliza Bahruji<sup>b</sup>, Peter J. Miedziak<sup>b,c</sup>, Thomas E. Davies<sup>b</sup>, David J. Morgan<sup>b</sup>, Samuel Pattison<sup>b</sup>, Sulawan Kaowphong<sup>a,d,e,\*</sup>, Graham J. Hutchings<sup>b,\*</sup>

<sup>a</sup> *Department of Chemistry, Faculty of Science, Chiang Mai University, Chiang Mai 50200, Thailand*

<sup>b</sup> *Cardiff Catalysis Institute, School of Chemistry, Cardiff University, Main Building, Park Place CF10 3AT, Cardiff, UK*

<sup>c</sup> *School of Applied Sciences, University of South Wales, Pontypridd CF37 4AT, UK*

<sup>d</sup> *Environmental Science Research Center (ESRC), Faculty of Science, Chiang Mai University, Chiang Mai 50200, Thailand*

<sup>e</sup> *Center of Excellence for Innovation in Chemistry, Faculty of Science, Chiang Mai University, Chiang Mai 50200, Thailand*

## Abstract

In this work, the biomolecule-assisted microwave heating synthesis of ZnIn<sub>2</sub>S<sub>4</sub>, along with the ZnIn<sub>2</sub>S<sub>4</sub>/MoS<sub>2</sub> composites and their photocatalytic applications, were studied. Well-defined flower-like ZnIn<sub>2</sub>S<sub>4</sub> microspheres synthesized at microwave heating time of 1 h provided the highest surface area and total pore volume, which offered the highest H<sub>2</sub> production rate (111.6 μmol h<sup>-1</sup> g<sup>-1</sup>). Different amounts of MoS<sub>2</sub> were loaded into the ZnIn<sub>2</sub>S<sub>4</sub> microspheres aiming to improve the H<sub>2</sub> production rate. Under UV-visible light irradiation, all ZnIn<sub>2</sub>S<sub>4</sub>/MoS<sub>2</sub> composites exhibited higher H<sub>2</sub> production rates than ZnIn<sub>2</sub>S<sub>4</sub> and MoS<sub>2</sub>, where the ZnIn<sub>2</sub>S<sub>4</sub>/MoS<sub>2</sub>-40% wt composite exhibited the highest H<sub>2</sub> production rate (200.1 μmol h<sup>-1</sup> g<sup>-1</sup>). In addition, for the first time, this composite was applied for the photoreduction reaction of Cr(VI) ion under visible light irradiation. It provided higher photoreduction efficiency than the single components, where the efficiency was improved in the acidic solutions over the levels recorded in the basic solution. The charge transfer pathway and photocatalytic mechanisms of the ZnIn<sub>2</sub>S<sub>4</sub>/MoS<sub>2</sub>-40% wt photocatalyst have been proposed based on the results obtained from UV-visible diffuse reflectance spectroscopy, photoluminescence spectroscopy, electrochemical impedance spectroscopy, Mott-Schottky measurements and the silver photo-deposition experiment.

**Keywords:** ZnIn<sub>2</sub>S<sub>4</sub>/MoS<sub>2</sub>, Microwave synthesis, Heterojunction, H<sub>2</sub> production, Cr(VI) reduction

## 1. Introduction

Photocatalytic production of H<sub>2</sub> gas from water splitting reactions and the reduction of heavy metal ions in the wastewater using solar energy in the presence of photocatalysts are effective strategies for resolving certain energy and environmental problems.<sup>1</sup> Semiconductor materials have attracted interest for use as photocatalysts for these photocatalytic reactions.

TiO<sub>2</sub> is known as the most efficient photocatalyst among various metal oxide semiconductors because of its high chemical stability, relatively low cost and non-toxic properties.<sup>2</sup> However, the practical applications of TiO<sub>2</sub> are limited by its poor visible light absorption capacity.<sup>3</sup> In pursuit of efficient utilization of solar energy, the exploration of highly active photocatalysts with visible light response is of great interest in current research studies. ZnIn<sub>2</sub>S<sub>4</sub>, the only member of AB<sub>2</sub>X<sub>4</sub> family semiconductors with a layered structure, has attracted considerable attention as a promising visible-light-driven photocatalyst for the photocatalytic reactions of H<sub>2</sub> evolution and Cr(VI) reduction due to its narrow band gap ( $E_g = 2.43\text{-}2.70$  eV) and good chemical stability.<sup>4 5 6</sup> However, it usually suffers from a high recombination rate of photo-generated charge carriers, which limits its photocatalytic efficiency.<sup>7</sup> There are several approaches that have been employed to improve the efficiency of ZnIn<sub>2</sub>S<sub>4</sub>, for example, the fabrication of ZnIn<sub>2</sub>S<sub>4</sub> with controllable morphology<sup>8 9</sup>, doping metal ions into the ZnIn<sub>2</sub>S<sub>4</sub> crystals<sup>10 11</sup> and by coupling ZnIn<sub>2</sub>S<sub>4</sub> with carbon<sup>12 13</sup> or fluoropolymer.<sup>14</sup> However, morphologically controlled strategies are practically difficult due to their complex formation mechanism, and the fact that the correlation between morphologies and the corresponding photocatalytic properties still remains unclear. High concentrations of transition metal ions lead to defects in the crystal lattice of ZnIn<sub>2</sub>S<sub>4</sub>.<sup>11</sup> Despite the recognition that coupling ZnIn<sub>2</sub>S<sub>4</sub> with carbon or fluoropolymer can enhance photocatalytic oxidation activity<sup>13</sup> and H<sub>2</sub> evolution<sup>14</sup>, and the fact that the photocorrosion of these composite photocatalysts can be prevented<sup>14</sup>, the electron-hole pair recombination process presents a major problem in terms of the decrease in the photocatalytic performance that still occur during the photocatalytic process.

Fabrication of a semiconductor heterostructure is a promising approach to inhibiting the electron-hole pair recombination process and to improving the efficiency of the photo-generated charge separation process.<sup>15</sup> Previously published literature has revealed that the ZnIn<sub>2</sub>S<sub>4</sub>/K<sub>2</sub>La<sub>2</sub>Ti<sub>3</sub>O<sub>10</sub> photocatalyst exhibited higher photocatalytic activity for H<sub>2</sub> evolution

when compared with ZnIn<sub>2</sub>S<sub>4</sub>.<sup>16</sup> However, K<sub>2</sub>La<sub>2</sub>Ti<sub>3</sub>O<sub>10</sub> is a wide-band-gap semiconductor ( $E_g = 3.05\text{-}3.50$  eV), which activates under the UV light region. Compared with metal oxide semiconductors, metal sulfides usually have narrower band gaps because they possess relatively high conduction band positions. These are consequently derived from the higher valence band position constructed by S 3*p* orbitals.<sup>17</sup> This entity enables them to absorb solar energy in the visible region. MoS<sub>2</sub> is a layer-structured transition metal dichalcogenide that has attracted attention as a photocatalyst for its role in the solar-driven H<sub>2</sub> evolution reaction and its role in hydrodesulfurization and hydrogenation due to its low cost, high chemical stability and excellent visible light response ( $E_g = 1.80$  eV).<sup>18 19 20</sup> Moreover, the conduction band position of MoS<sub>2</sub> was less negative than the hexagonal ZnIn<sub>2</sub>S<sub>4</sub> material.<sup>21</sup> Therefore, the possibility for a directional transfer of the photo-generated electrons from ZnIn<sub>2</sub>S<sub>4</sub> to MoS<sub>2</sub> is feasible. Consequently, the photo-generated holes would move in the opposite direction. As a result of these actions, the photo-generated charge recombination process could effectively be inhibited. In addition, a typical layered structure of MoS<sub>2</sub> assists a good interfacial contact on the ZnIn<sub>2</sub>S<sub>4</sub> surface, which is one of the important factors facilitating the promotion of the photo-generated electrons and holes to transfer across the contact interface between ZnIn<sub>2</sub>S<sub>4</sub> and MoS<sub>2</sub> in the ZnIn<sub>2</sub>S<sub>4</sub>/MoS<sub>2</sub> heterostructure. This then leads to an increase in the photocatalytic H<sub>2</sub> evolution activity as has been previously reported in published literatures.<sup>7</sup>

21, 22 23 24 25

The microwave heating synthesis method is a low-energy method requiring rapid heating. It has strong potential to synthesize semiconductor materials with a high degree of crystallinity and purity. In a comparison with conventional heating methods, the microwave heating method involves a conversion from electromagnetic energy to thermal energy rather than a transfer of heat. It requires the microwave absorption ability of conductive substances and solvent in the reaction solution. During microwave irradiation, microwave energy interacts

directly with these substances through a molecular interaction with the electromagnetic field, resulting in a degree of volumetric heating that allows rapid and more uniform heating.<sup>26</sup> Consequently, the highly crystalline materials with uniformed shape and narrow size distribution can be obtained at a relatively low temperature and over a short period of time.<sup>27</sup> This leads to a significant reduction in energy consumption in terms of material production. Moreover, by utilizing microwave radiation, semiconductor-based composite materials, with a strong interaction of two single-materials, can be successfully achieved.<sup>28</sup>

Recently, biomolecule-assisted synthesis has become an environmentally friendly route for preparing various metal sulfide semiconductors.<sup>29 30</sup> Herein, L-cysteine, an inexpensive and simple amino acid, has been chosen as a sulfur source because the characteristic functional groups in its molecular structure, including the simple hydrosulfide group (-SH) and the multifunctional groups (-NH<sub>2</sub> and -COO<sup>-</sup>), can coordinate with metal ions to form metal-L-cysteine complexes. Subsequently, sulfur ion (S<sup>2-</sup>) is released.<sup>31 32 33</sup> Thus, the formation of toxic H<sub>2</sub>S gas as a result of the employment of a familiar sulfur source (thioacetamide, thiourea, sodium thiosulfate and Na<sub>2</sub>S) can be prevented.<sup>34</sup>

In this work, the biomolecule-assisted microwave heating method using L-cysteine as a sulfur source was applied for the fabrication of ZnIn<sub>2</sub>S<sub>4</sub> and ZnIn<sub>2</sub>S<sub>4</sub>/MoS<sub>2</sub> materials. First, the microwave heating time was verified in order to investigate the characteristics and photocatalytic H<sub>2</sub> production of ZnIn<sub>2</sub>S<sub>4</sub> under UV-visible light irradiation. Additionally, different weight percentages of MoS<sub>2</sub> were then loaded into ZnIn<sub>2</sub>S<sub>4</sub> to form ZnIn<sub>2</sub>S<sub>4</sub>/MoS<sub>2</sub> composites with the goal of enhancing the H<sub>2</sub> production rate. Moreover, the ZnIn<sub>2</sub>S<sub>4</sub>/MoS<sub>2</sub> composite with an optimum weight percentage of MoS<sub>2</sub> was applied for a reduction reaction of a toxic Cr(VI) ion to a less toxic Cr(III) ion under visible light irradiation, in parallel with ZnIn<sub>2</sub>S<sub>4</sub>, MoS<sub>2</sub>, and physical mixture of ZnIn<sub>2</sub>S<sub>4</sub> and MoS<sub>2</sub>. In addition, the photocatalytic stability of the ZnIn<sub>2</sub>S<sub>4</sub>/MoS<sub>2</sub> photocatalyst under the same reaction conditions was

investigated. Possible photocatalytic mechanisms for the enhancement of H<sub>2</sub> production and Cr(VI) reduction reactions over the ZnIn<sub>2</sub>S<sub>4</sub>/MoS<sub>2</sub> composite have also been discussed.

## 2. Materials and methods

### 2.1. Photocatalysts preparation

For the synthesis of ZnIn<sub>2</sub>S<sub>4</sub>, ZnCl<sub>2</sub> (2.0 mmol; Sigma-Aldrich, 99.99%), InCl<sub>3</sub>·4H<sub>2</sub>O (4.0 mmol; Sigma-Aldrich, 97.0%) and L-cysteine (10.0 mmol; Sigma-Aldrich, 97.0%) were dissolved in de-ionized water (20.0 mL). After constant stirring for 20 min, the solution was transferred into a dissolution vessel with a capacity of 50.0 mL. The vessel was sealed and exposed to microwave radiation at 100 W in a microwave synthesis reactor (Discover SP Installation, Model PN600635) and then naturally cooled to room temperature. The microwave heating time was varied from 1 to 3 h. Finally, a dark green-yellow powder was collected by vacuum filtration, washed several times with de-ionized water and dried (80 °C for 24 h).

For the synthesis of MoS<sub>2</sub>, Na<sub>2</sub>MoO<sub>4</sub>·2H<sub>2</sub>O (2.0 mmol; Merck, 99.5%) and L-cysteine (4.0 mmol; Sigma-Aldrich, 97.0%) were dissolved in de-ionized water (50.0 mL). After constant stirring for 20 min, the solution was transferred into a Teflon-lined stainless-steel autoclave with a capacity of 125.0 mL. The autoclave was sealed and heated (200 °C for 24 h) and then naturally cooled to room temperature. Finally, a black powder was separated from the mother liquor by vacuum filtration, washed several times with de-ionized water and dried (80 °C for 24 h).

To synthesize ZnIn<sub>2</sub>S<sub>4</sub>/MoS<sub>2</sub> composites, the as-prepared ZnIn<sub>2</sub>S<sub>4</sub> and MoS<sub>2</sub> powders were dispersed in de-ionized water (20.0 mL) under constant stirring. The suspension was then transferred into a dissolution vessel with a capacity of 50.0 mL. The vessel was sealed and exposed to microwave radiation in the microwave synthesis reactor operated at 100 W for 1 h

and then naturally cooled to room temperature. Finally, the resulting powder was collected by centrifugation and then dried (80 °C for 24 h). The ZnIn<sub>2</sub>S<sub>4</sub>/MoS<sub>2</sub> composites with different loading amounts of MoS<sub>2</sub> were denoted as ZIS/MS-x%, where x represents the weight percentage of MoS<sub>2</sub> (20, 30, 40, 50, 60 and 80). A physical mixture of ZnIn<sub>2</sub>S<sub>4</sub> and 40% wt of MoS<sub>2</sub>, denoted as mixed-40%, was also prepared by physical grinding without microwave treatment for the purposes of comparison.

## 2.2. Photocatalyst characterization techniques

The X-ray diffraction (XRD) patterns were obtained using a RIGAKU Smartlab X-ray diffractometer with CuK<sub>α</sub> radiation (40 kV and 40 mA) and Ni attenuator. UV-visible diffuse reflectance spectroscopy (UV-visible DRS, Agilent Technologies, Cary Series) was used to record the UV-visible DRS spectra in a wavelength range of 200-800 nm with a scan rate of 150 nm/min. The Brunauer-Emmett-Teller N<sub>2</sub> gas adsorption method (BET, Quantachrome, Quadrasorb-*evo*) was used to determine the specific surface area and pore volume of the solid samples, where water adsorbed on the surface of samples was removed at 120 °C for 3 h under a vacuum before analysis. Particle size and morphology were analyzed using a scanning electron microscope (SEM, TESCAN MAIA3 and JEOL JSM-6335 F). The microstructure was analyzed with a transmission electron microscope (TEM, JEOL, JEM-2010). Energy-dispersive X-ray spectroscopy (EDX) was used in conjunction with SEM and with TEM to analyze elemental compositions of the sample. To determine the oxidation states of the elements on the surface of the samples, the X-ray photoelectron spectra (XPS, Kratos Axis Ultra DLD) were recorded using AlK<sub>α</sub> irradiation at 120 W and analyzer pass energies of 160 eV. The photoluminescence spectra (PL, Avantes AvaSpec-2048TEC-USB2) were recorded with an excitation wavelength of 590 nm at room temperature. Time-resolved

photoluminescence (TRPL) decay spectra were recorded on a DeltaFlex Lifetime Spectrofluorometer.

Electrochemical measurements (Autolab Potentiostat/galvonostat, PGSTAT128N, Metrohm Siam Ltd.) were performed using a three-electrode cell and Na<sub>2</sub>SO<sub>4</sub> aqueous solution (0.1 M), which served as an electrolyte solution. To fabricate a working electrode, the photocatalyst (0.1 g) was dispersed in 10.0 mL of a solution of isopropanol and DI water (40:20 % v/v) under magnetic stirring. Subsequently, the dispersion solution was dropped on the fixed area (1x1 cm<sup>2</sup>) of a fluorine-doped tin oxide (FTO) coated glass substrate. After overnight evaporation (60 °C), a working electrode was obtained. Platinum (Pt) and Ag/AgCl were used as counter and reference electrodes, respectively. The electrochemical impedance spectra (EIS) were recorded by imposing a voltage of 1.5 V within a frequency range from 0.1 Hz-100 kHz. Linear sweep voltammograms were performed under visible light irradiation for 180 s, operating at 200 mV/s in a range from -0.4 V to +1.3 V (*vs.* Ag/AgCl). The transient photocurrent response was measured in a light on-off process with a pulse of 30 s and bias potential of 1.0 V. The Mott-Schottky plots were performed at a range of -1.5 V to +1.5 V (*vs.* Ag/AgCl) with an applied frequency of 100 Hz and an AC amplitude of 10 mV. To convert the measured potential *vs.* Ag/AgCl to the NHE scale, the following equation was applied;  $E_{NHE} = E_{Ag/AgCl} + E^{\circ}_{Ag/AgCl}$ , where  $E^{\circ}_{Ag/AgCl}$  (3.0 M KCl) = 0.21 V at 25 °C.

### 2.3. Experimental setup for photocatalytic reaction tests

Photocatalytic measurement for the H<sub>2</sub> production reaction was performed in a closed Pyrex flask reactor (150 mL). The photocatalyst (0.1 g) was dispersed in 100.0 mL of a mixed aqueous solution containing Na<sub>2</sub>S (0.35 M) and Na<sub>2</sub>SO<sub>3</sub> (0.25 M) as a sacrificial reagent. The volume ratio of the Na<sub>2</sub>S/Na<sub>2</sub>SO<sub>3</sub> sacrificial reagent and de-ionized water was 60:40 v/v. Prior to irradiation, the suspension was purged with argon gas for 30 min to remove the dissolved

gases in the de-ionized water. The photocatalytic reaction was carried out for 3 h by irradiating the suspension with a Xenon lamp (150 W, Oriel Model 6256, Newport) that was positioned 10.0 cm from the reactor. The spectral irradiance of the Xenon lamp is shown in Fig. S1. During light irradiation, continuous magnetic stirring was applied to sustain the photocatalyst in the suspension. The evolved H<sub>2</sub> amount was monitored with a gas chromatograph (PerkinElmer, Clarus 480) equipped with a packed 13X molecular sieve column and a thermal conductivity detector (with argon gas as the carrier gas).

For the photocatalytic Cr(VI) reduction test, an LED white light (50 W YNL Model COB) was used as a visible light source that was located 8.0 cm from the reactor.<sup>28</sup> The spectral irradiance of the LED lamp is shown in Fig. S2. The photocatalyst (0.1 g) was dispersed in a K<sub>2</sub>Cr<sub>2</sub>O<sub>7</sub> aqueous solution (10 ppm, 200.0 mL). The pH value of the solution was adjusted using 1 M HCl or 1 M NH<sub>4</sub>OH solutions. Before light irradiation, the suspension was magnetically stirred in the dark for 30 min to reach adsorption-desorption equilibrium. During light irradiation, the suspension (5 mL) was sampled every 30 min. Finally, the Cr(VI) content in the sampling was measured colorimetrically using the standard diphenylcarbazide method.<sup>35</sup> In this method, Cr(VI) ion reacts with 1,5-diphenylcarbazide under acidic condition<sup>28</sup> resulting in the formation of a reddish-purple-colored complex of a Cr(VI)-diphenylcarbazide complex. This process can be monitored using UV-visible spectroscopy at  $\lambda_{\max}$  of 532 nm. The photoreduction efficiency was calculated using the following equation;

$$\%Photoreduction\ efficiency = \left[ \frac{C_0 - C}{C_0} \right] \times 100$$

where C<sub>0</sub> and C were the concentrations of the Cr(VI) complex at adsorption-desorption equilibrium and after light irradiation, respectively. A blank experiment (without adding any photocatalyst) was also carried out under the same conditions for the purposes of comparison.

Apparent quantum yield (AQY) of ZnIn<sub>2</sub>S<sub>4</sub> and ZnIn<sub>2</sub>S<sub>4</sub>/MoS<sub>2</sub>-40% wt photocatalysts for the H<sub>2</sub> production and Cr(VI) production reactions were also calculated. The calculation

methods are presented in the Supporting Information. The photocatalyst powders after the photocatalytic reaction tests were carefully recovered by centrifugation and by washing them several times with de-ionized water. After being dried at 60 °C, the recovered photocatalysts were reused to assess further photocatalytic reactions under the same experimental conditions.

### 3. Results and discussion

#### 3.1. Effect of microwave heating time on the characteristics and photocatalytic H<sub>2</sub> production rate of ZnIn<sub>2</sub>S<sub>4</sub>

XRD patterns of the powders synthesized at different microwave heating times are shown in Fig. S3. The main diffraction peaks located at  $2\theta$  of 21.2°, 27.9°, 30.1°, 39.9°, 47.3°, 51.8° and 55.5° correspond to the (006), (102), (104), (108), (110), (116) and (202) crystal planes of the hexagonal ZnIn<sub>2</sub>S<sub>4</sub> phase (JCPDS no. 01-072-0773). No other diffraction peaks of any possible impurities, such as binary metal sulfide and metal oxide related to the precursors, are observed.<sup>36</sup> The strong and sharp diffraction peaks indicate that the synthesized ZnIn<sub>2</sub>S<sub>4</sub> powders are well-crystalline.<sup>37</sup> With prolonged microwave heating times, the (104) crystal plane is strengthened suggesting an increase in the degree of crystallinity of ZnIn<sub>2</sub>S<sub>4</sub>. The crystallite size of the ZnIn<sub>2</sub>S<sub>4</sub> particles was calculated from the (110) diffraction peak by applying the Debye-Scherrer equation;  $D = 0.9\lambda/\beta\cos\theta$ , where  $D$  is the crystallite size in nanometer,  $\lambda$  is the wavelength of CuK $\alpha$ ,  $\beta$  is the full width at half-maximum (FWHM) in radian and  $\theta$  is the half-diffraction angle in degrees.<sup>38</sup> The calculated crystallite size of the ZnIn<sub>2</sub>S<sub>4</sub> particles synthesized at 1 h, 2 h and 3 h are 19.6, 48.0 and 86.3 nm, respectively. These results imply that microwave heating time affects the crystallinity and crystallite size of ZnIn<sub>2</sub>S<sub>4</sub> synthesized under the present synthesis conditions.

UV-visible DRS spectra of all ZnIn<sub>2</sub>S<sub>4</sub> powders (Fig. 1a) show the absorption edges at 440 nm, 470 nm and 480 nm, respectively. According to the equation  $E_g = 1240/\lambda$ , where the  $E_g$  and  $\lambda$  represent the band gap energy and absorption edge of semiconductors, the band gap energy values of ZnIn<sub>2</sub>S<sub>4</sub> are 2.81, 2.64 and 2.58 eV for the ZnIn<sub>2</sub>S<sub>4</sub> powders synthesized at 1 h, 2 h and 3 h, respectively. These findings imply that all synthesized ZnIn<sub>2</sub>S<sub>4</sub> powders are visible-light active materials. Fig. 1b-1d presents the high-resolution XPS spectra of Zn 2p, In 3d and S 2p of the ZnIn<sub>2</sub>S<sub>4</sub> samples. The XPS spectra of Zn 2p (Fig. 1b) reveal two peaks of Zn 2p<sub>3/2</sub> and Zn 2p<sub>1/2</sub> centered at 1022.08 eV and 1048.08 eV, respectively. The XPS spectra of In 3d (Fig. 1c) show two peaks centered at 445.08 eV and 452.20 eV which are indexed as the binding energy values of In 3d<sub>5/2</sub> and In 3d<sub>3/2</sub>, respectively. The XPS spectra of S 2p (Fig. 1d) can be convoluted into two peaks; one is located at 161.83 eV (S 2p<sub>1/2</sub>) and the other is at 162.93 eV (S 2p<sub>3/2</sub>). The binding energy values correspond to the oxidation states of Zn<sup>2+</sup>, In<sup>3+</sup> and S<sup>2-</sup>, respectively.<sup>39</sup> The gradually decrease in the XPS intensity with prolonging microwave reaction time could be attributed to the decrease in the atomic concentration of metals at the surface of ZnIn<sub>2</sub>S<sub>4</sub> as presented in Fig. S4 and the diffusion of metal atoms towards the bulk.

40, 41

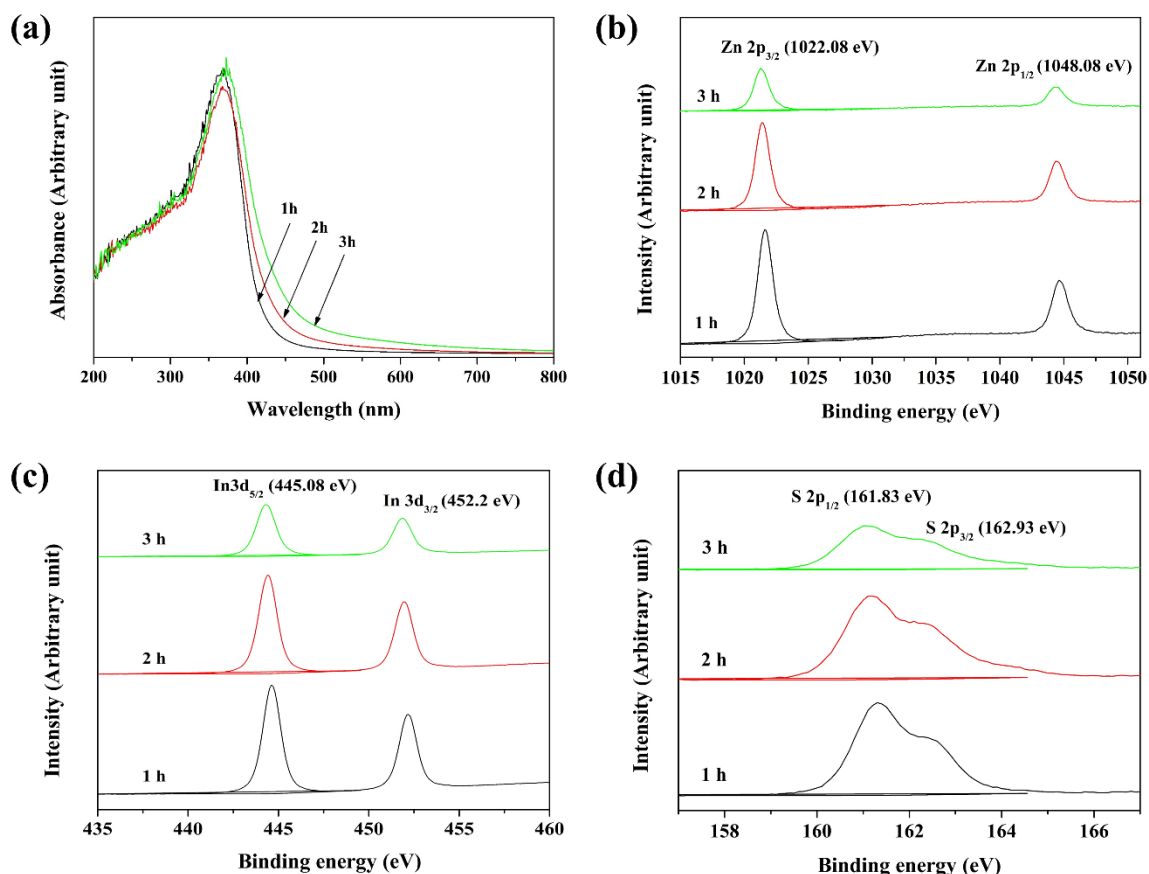


**Fig. 1.** (a) UV-visible DRS spectra and high-resolution XPS spectra of (b) Zn 2p, (c) In 3d and (d) S 2p of the  $\text{ZnIn}_2\text{S}_4$  powders synthesized at different microwave heating times.

SEM images of all  $\text{ZnIn}_2\text{S}_4$  powders (Fig. 2) reveal that the powder synthesized at 1 h (Fig. 2a) is composed of flower-like microspheres with an average diameter of 2  $\mu\text{m}$ . These microspheres are constructed of several interconnected nanosheets with an average thickness of 50 nm, creating multi-cavities on their surface. With longer heating times applied, flower-like  $\text{ZnIn}_2\text{S}_4$  microspheres still obtained but the diameter size is increased, and an aggregation behavior is observed (Fig. 2a-2c). The average diameters of such microspheres are 4 and 6  $\mu\text{m}$  for  $\text{ZnIn}_2\text{S}_4$  synthesized at 2 and 3 h, respectively. In addition, the merging of the adjacent nanosheets is observed leading to a decrease in the number of the cavities on the surface of the microspheres. These phenomena probably occur as a result of the behavior of the particles and

their tendency to reduce excess energy at the surface, which is activated by microwave radiation during the prolonged irradiation. The BET surface areas of the ZnIn<sub>2</sub>S<sub>4</sub> microspheres synthesized at 1 h, 2 h and 3 h are 48, 42 and 39 m<sup>2</sup> g<sup>-1</sup>, respectively. The N<sub>2</sub> adsorption-desorption isotherms of these samples are provided in Fig. S5a. Additionally, total pore volumes of ZnIn<sub>2</sub>S<sub>4</sub> synthesized at 1 h, 2 h and 3 h are 0.2877, 0.2609 and 0.1868 cm<sup>3</sup> g<sup>-1</sup>, respectively. The BET surface area and total pore volumes decrease along with an increase in the microwave heating time, which are consistent with the decrease in the number of cavities on the surface of ZnIn<sub>2</sub>S<sub>4</sub> microspheres as can be observed in the SEM images (Fig. 2d-2f).

The photocatalytic H<sub>2</sub> production rates of all ZnIn<sub>2</sub>S<sub>4</sub> powders were investigated under UV-visible light irradiation. The amounts of produced H<sub>2</sub> gas were plotted as a function of time (Fig. 2g). The ZnIn<sub>2</sub>S<sub>4</sub> photocatalysts synthesized at 1, 2 and 3 h can produce H<sub>2</sub> gas at the rates of 111.6, 50.6 and 36.2 μmol h<sup>-1</sup> g<sup>-1</sup>, respectively. The ZnIn<sub>2</sub>S<sub>4</sub> photocatalyst synthesized at 1 h provides the highest rate of H<sub>2</sub> production. Consequently, it is suggested that the greater the surface area and total pore volume of the photocatalyst not only provide more available active sites for the adsorption of substrates on the surface of the photocatalyst, but also increase surface charge carriers that are transferred during the H<sub>2</sub> production process.<sup>42</sup> Additionally, the large number of cavities on the surface of the ZnIn<sub>2</sub>S<sub>4</sub> photocatalyst could promote multiple reflections and the scattering of the incident light on their surface, resulting in an improvement in light harvesting efficiency and an increase in the life-time of the photo-generated charge carriers that take part in the photocatalytic reactions.<sup>43 44</sup> In addition, the larger band gap energy of the ZnIn<sub>2</sub>S<sub>4</sub> photocatalyst that was synthesized at 1 h could hinder the rate of electron-hole pair recombination in the ZnIn<sub>2</sub>S<sub>4</sub> structure.<sup>45</sup> Furthermore, the atomic concentration of the metals at the surface of ZnIn<sub>2</sub>S<sub>4</sub> could be one of the factors affecting to its photocatalytic activity. Based on these results, the ZnIn<sub>2</sub>S<sub>4</sub> powder that was synthesized at 1 h was chosen to

be combined with different loading amounts of MoS<sub>2</sub> to form the ZnIn<sub>2</sub>S<sub>4</sub>/MoS<sub>2</sub> composites in an attempt to improve its overall photocatalytic activity.

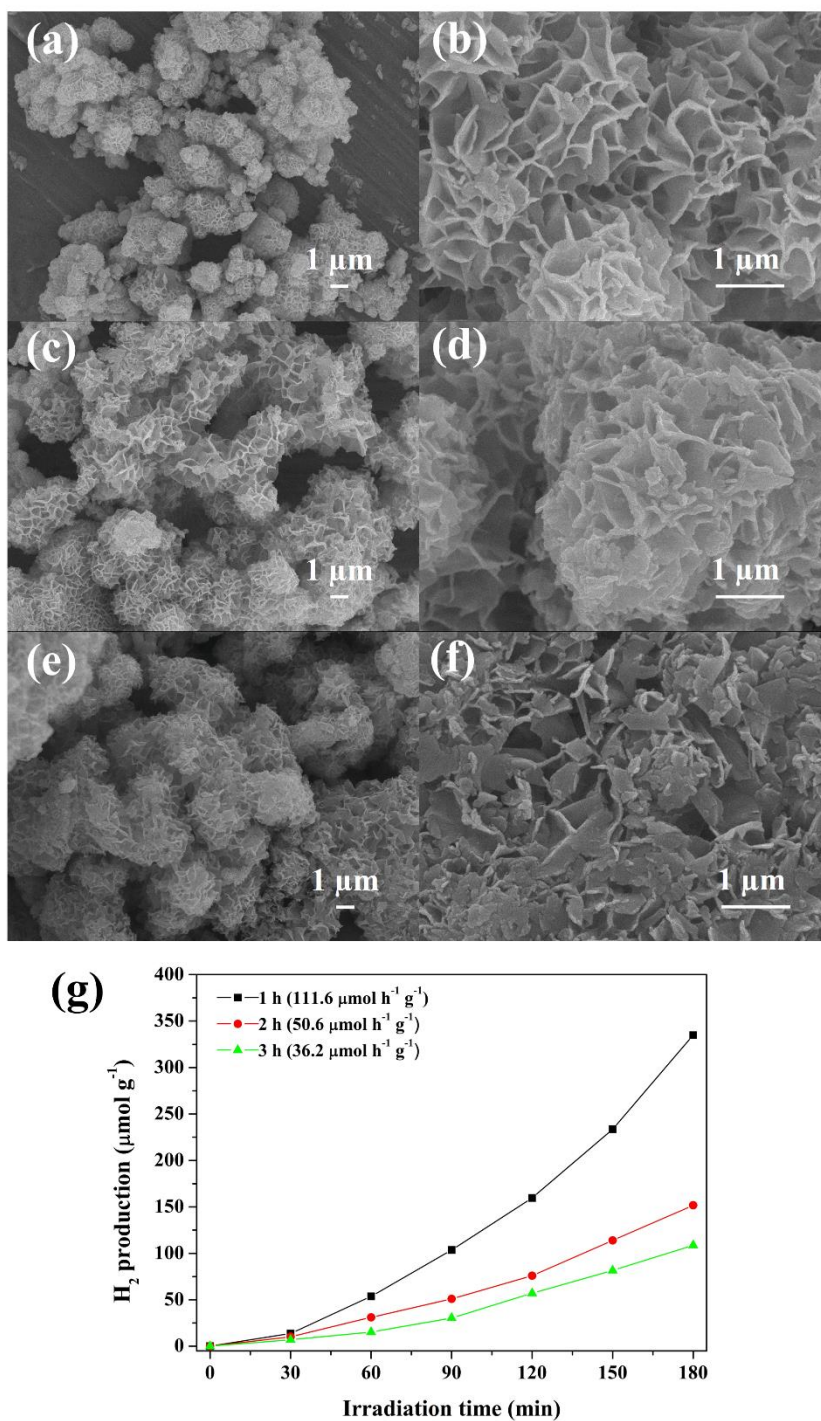


**Fig. 2.** SEM images of the ZnIn<sub>2</sub>S<sub>4</sub> powders synthesized at (a and d) 1 h, (b and e) 2 h and (c and f) 3 h. (g) The H<sub>2</sub> production rate of the ZnIn<sub>2</sub>S<sub>4</sub> photocatalysts.

## 3.2. Photocatalytic activity of ZnIn<sub>2</sub>S<sub>4</sub>/MoS<sub>2</sub> composites

### 3.2.1. Characterizations of some synthesized samples

The XRD spectrum of the ZnIn<sub>2</sub>S<sub>4</sub>/MoS<sub>2</sub>-40% wt composite shown in Fig. 3a exhibits the diffraction peaks of the hexagonal ZnIn<sub>2</sub>S<sub>4</sub> structure with additional diffraction peaks located at  $2\theta$  of 14.4° and 33.5°, which can be indexed as the (002) and (101) crystal planes of the hexagonal MoS<sub>2</sub> structure (JCPDS no. 01-075-1539), respectively. This result suggests the successful fabrication of the ZnIn<sub>2</sub>S<sub>4</sub>/MoS<sub>2</sub> composite via the microwave heating method. The spectrum of the composite is not changed in terms of the peak positions and shapes when compared with those of ZnIn<sub>2</sub>S<sub>4</sub>, indicating that the existence of MoS<sub>2</sub> does not affect the crystal structure of ZnIn<sub>2</sub>S<sub>4</sub>. The peak intensity of ZnIn<sub>2</sub>S<sub>4</sub> in the ZnIn<sub>2</sub>S<sub>4</sub>/MoS<sub>2</sub>-40% wt composite decreases after being combined with MoS<sub>2</sub>. This result implies that the ZnIn<sub>2</sub>S<sub>4</sub> particles can be deposited by the MoS<sub>2</sub> particles, which can then be further confirmed by SEM and TEM analyses. UV-visible DRS spectrum of the ZnIn<sub>2</sub>S<sub>4</sub>/MoS<sub>2</sub>-40% wt composite in comparison with ZnIn<sub>2</sub>S<sub>4</sub> and MoS<sub>2</sub> is shown in Fig. 3b. MoS<sub>2</sub> has an absorption edge at 630 nm corresponding to a band gap energy of 1.96 eV (inset of Fig. 3b). After introducing MoS<sub>2</sub> to ZnIn<sub>2</sub>S<sub>4</sub>, the absorption edge of ZnIn<sub>2</sub>S<sub>4</sub>/MoS<sub>2</sub>-40% wt shifts to longer wavelength region when compared with that of ZnIn<sub>2</sub>S<sub>4</sub>, and the absorption ability of the composite in the visible light region is enhanced. These results imply that the ZnIn<sub>2</sub>S<sub>4</sub>/MoS<sub>2</sub> composite can utilize more visible light to generate more electrons and holes. Consequently, the enhancement of the visible-light absorption ability of this composite could be attributed to the interaction between ZnIn<sub>2</sub>S<sub>4</sub> and MoS<sub>2</sub>, which can then be further confirmed by XPS analysis.

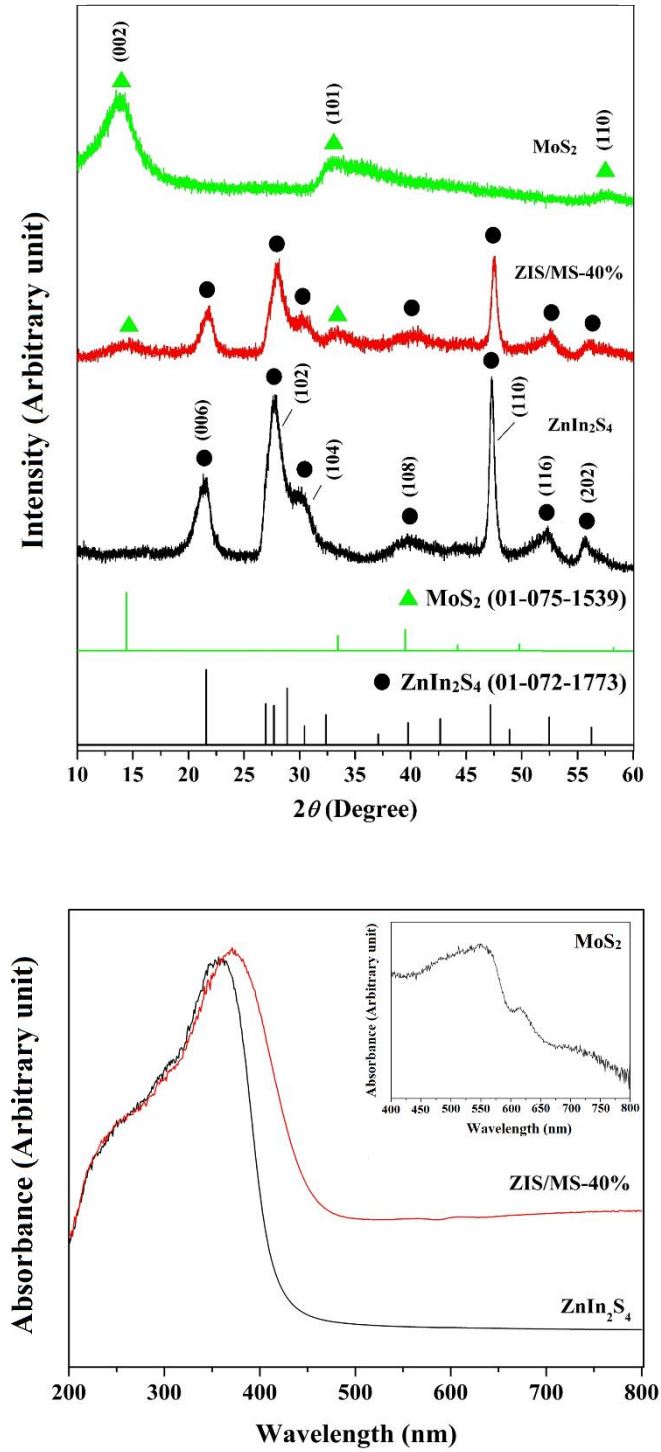


**Fig. 3.** (a) XRD patterns and (b) UV-visible DRS spectra of the ZnIn<sub>2</sub>S<sub>4</sub>, MoS<sub>2</sub> powders and the ZnIn<sub>2</sub>S<sub>4</sub>/MoS<sub>2</sub>-40% wt composite.

The high-resolution XPS spectra of Zn 2p, In 3d, S 2p and Mo 3d for the ZnIn<sub>2</sub>S<sub>4</sub>/MoS<sub>2</sub>-40% wt composite in comparison with those of the ZnIn<sub>2</sub>S<sub>4</sub> and MoS<sub>2</sub> are displayed in Fig. 4. The XPS signals for Zn 2p of the composite (Fig. 4a) reveal that the peaks at 1022.18 and 1048.23 eV correspond to Zn 2p<sub>3/2</sub> and Zn 2p<sub>1/2</sub>, respectively, suggesting the +2 oxidation state of Zn. The signals of In 3d (Fig. 4b) at binding energy values of 445.38 and 452.58 eV correspond to In 3d<sub>5/2</sub> and In 3d<sub>3/2</sub>, respectively, indicating the presence of In<sup>3+</sup>. The spectrum of S 2p (Fig. 4c) shows that the peaks at 161.98 and 162.98 eV are attributed to S 2p<sub>3/2</sub> and S 2p<sub>1/2</sub>, confirming the -2 oxidation state of S. In Fig. 4d, the peaks at binding energy values of 232.13 eV and 228.78 eV are assigned to Mo 3d<sub>5/2</sub> and Mo 3d<sub>3/2</sub>, respectively, which correspond to the +4 oxidation state of Mo.<sup>46</sup> Additionally, the peak at 226.28 eV corresponds to the S 2s transition. The XPS result confirms that the prepared ZnIn<sub>2</sub>S<sub>4</sub>/MoS<sub>2</sub> is indeed a composite of ZnIn<sub>2</sub>S<sub>4</sub> and MoS<sub>2</sub>. It is also found that these binding energy values shift in comparison to ZnIn<sub>2</sub>S<sub>4</sub> and MoS<sub>2</sub>, indicating the changes in the chemical environments of Zn<sup>2+</sup>, In<sup>2+</sup> ions in ZnIn<sub>2</sub>S<sub>4</sub> structure and Mo<sup>4+</sup> ion in MoS<sub>2</sub> structure. This finding implies a chemical interaction between ZnIn<sub>2</sub>S<sub>4</sub> and MoS<sub>2</sub> at the interfacial of the ZnIn<sub>2</sub>S<sub>4</sub>/MoS<sub>2</sub> heterostructure after the microwave treatment **rather than a physical interaction**.

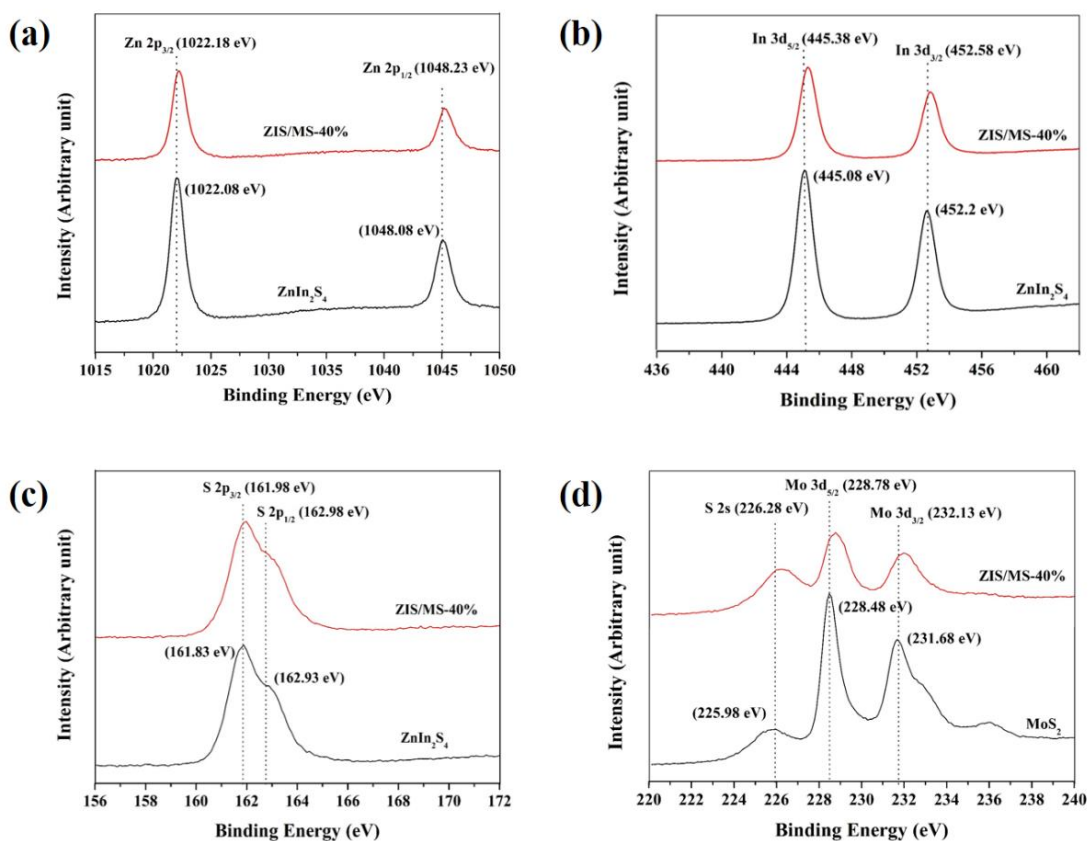


**Fig. 4.** High-resolution XPS spectra of (a) Zn 2p, (b) In 3d (c) S 2p and (d) Mo 4f of  $\text{ZnIn}_2\text{S}_4/\text{MoS}_2$ -40% wt in comparison with  $\text{ZnIn}_2\text{S}_4$  and  $\text{MoS}_2$ .

The SEM images of  $\text{ZnIn}_2\text{S}_4$ ,  $\text{MoS}_2$  and  $\text{ZnIn}_2\text{S}_4/\text{MoS}_2$ -40% wt are shown in Fig. 5. The morphology of  $\text{MoS}_2$  (Fig. 5b) seems to be a cluster-like structure with an average diameter size of 350 nm. This structure is constructed of highly aggregated ultrathin nanosheets (inset of Fig. 5b). It is also found that the  $\text{MoS}_2$  nanosheets are curved, which is similar to the previously reported features of  $\text{MoS}_2$ .<sup>47</sup> This phenomena could be attributed to the fact that ultrathin nanosheets are unstable and closed structures can easily be formed by rolling up to eliminate dangling bonds at the edges and to minimize their surface energy.<sup>48,49</sup> The SEM (Fig. 5c and 5d) and TEM (Fig. 5e and 5f) images of the composite reveal that the  $\text{MoS}_2$  particles cover the surface of the  $\text{ZnIn}_2\text{S}_4$  nanosheets and are also deposited on the interior surface of

the cavities. The BET surface areas of the  $\text{ZnIn}_2\text{S}_4$ ,  $\text{ZnIn}_2\text{S}_4/\text{MoS}_2$ -40%wt and  $\text{MoS}_2$  are 48, 40 and  $8 \text{ m}^2 \text{ g}^{-1}$  with the total pore volumes of 0.2877, 0.1798 and  $0.032 \text{ cm}^3 \text{ g}^{-1}$ , respectively. The  $\text{N}_2$  adsorption-desorption isotherm of  $\text{ZnIn}_2\text{S}_4/\text{MoS}_2$ -40%wt in comparison with  $\text{ZnIn}_2\text{S}_4$  is provided in Fig. S5b. The high-magnified TEM image of the composite (Fig. 5g-5h) reveals lattice fringes of 0.42 nm and 0.22 nm, which can be indexed as (006) plane of  $\text{ZnIn}_2\text{S}_4$  and (103) plane of  $\text{MoS}_2$ , respectively. This finding implies the highly crystalline nature of the composite material and confirms that the  $\text{ZnIn}_2\text{S}_4/\text{MoS}_2$  heterojunction is formed through the close contact between the  $\text{ZnIn}_2\text{S}_4$  and  $\text{MoS}_2$  particles. The EDX spectrum of the  $\text{ZnIn}_2\text{S}_4/\text{MoS}_2$ -40%wt composite (Fig. 6a) reveals the characteristic signals of the Zn, In, S and Mo elements, further confirming the existence of both  $\text{ZnIn}_2\text{S}_4$  and  $\text{MoS}_2$  in the  $\text{ZnIn}_2\text{S}_4/\text{MoS}_2$ -40%wt composite. Notably, the signals of the C and O elements are found to have come from the environment. Scanning TEM-EDX elemental mapping (Figs. 6b-6f) reveals that the Zn, In, S and Mo elements are homogeneously distributed throughout the composite material. This suggests that the porous structure of  $\text{ZnIn}_2\text{S}_4$  facilitates the formation of the interfacial heterostructure between  $\text{ZnIn}_2\text{S}_4$  and  $\text{MoS}_2$  after being exposed to microwave radiation.<sup>50</sup> Based on the chemical compositions obtained from the EDX analysis, the actual weight percentage of  $\text{MoS}_2$  in the  $\text{ZnIn}_2\text{S}_4/\text{MoS}_2$ -40%wt composite was calculated to be 39.45%, which is close to the preparation content.

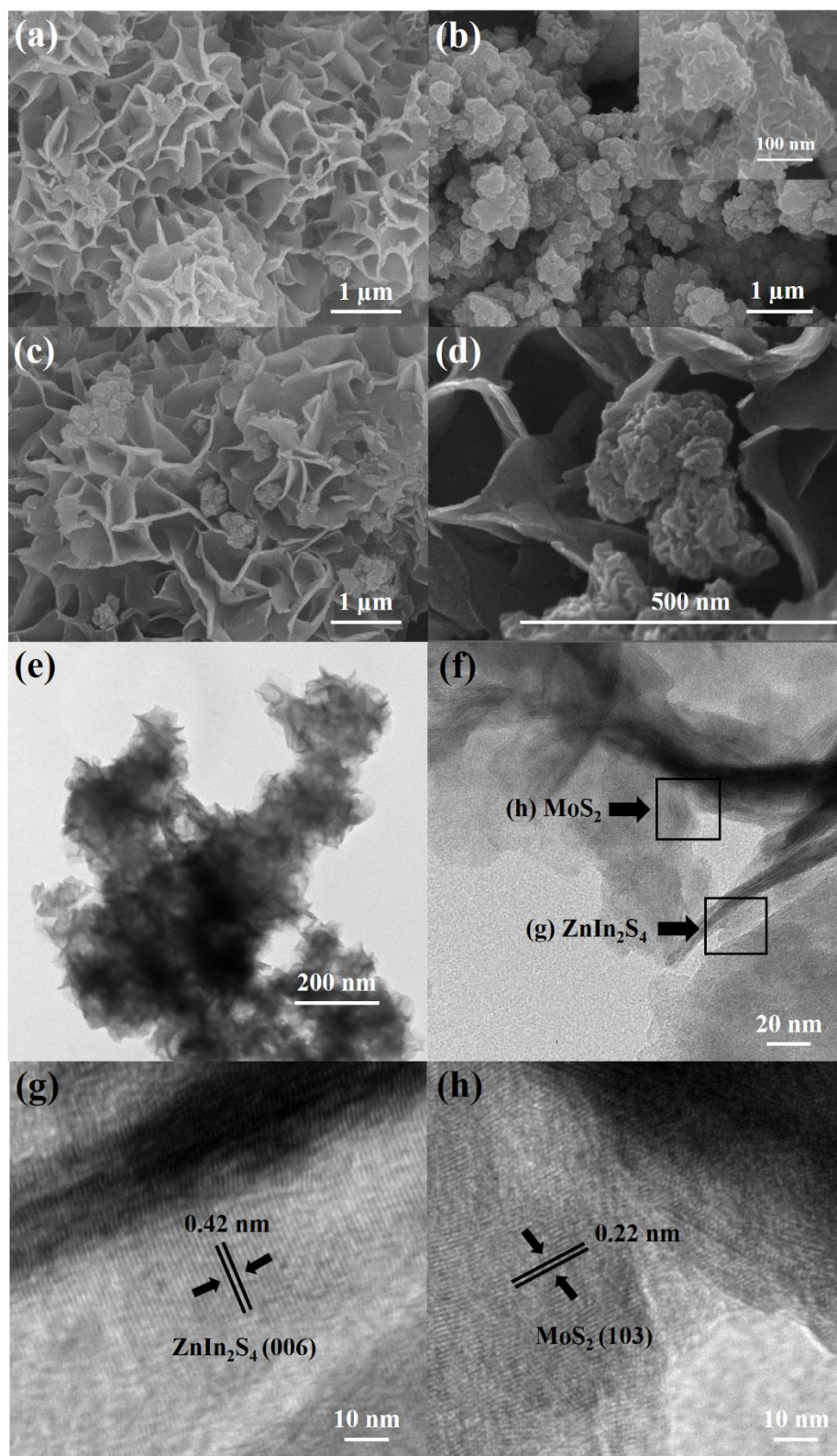


**Fig. 5.** SEM images of (a)  $\text{ZnIn}_2\text{S}_4$ , (b)  $\text{MoS}_2$  and (c)  $\text{ZnIn}_2\text{S}_4/\text{MoS}_2$ -40% wt. (e-f) TEM images of  $\text{ZnIn}_2\text{S}_4/\text{MoS}_2$ -40% wt. (g-h) High-magnified TEM images (x 600,000 magnification) of the selected square area shown in (f).

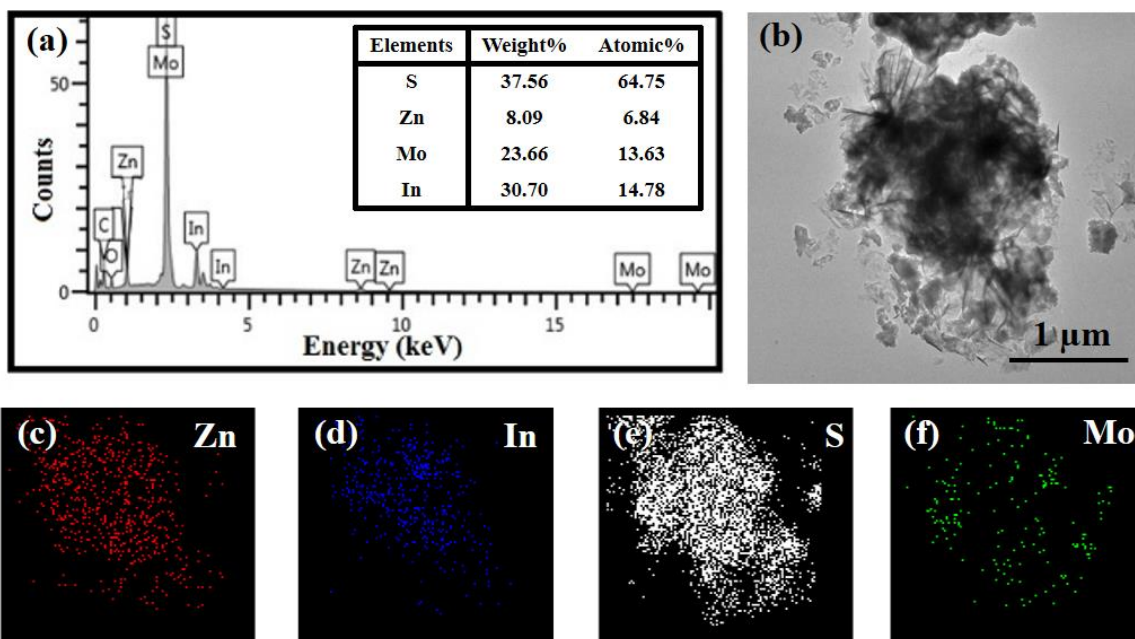


**Fig. 6.** (a) EDX spectrum with chemical compositions, and (b) STEM image and (c-f) the corresponding EDX elemental mapping images of the  $\text{ZnIn}_2\text{S}_4/\text{MoS}_2$ -40%wt composite.

The EIS Nyquist plots can be used to determine the charge transfer resistance and the separation efficiency of photo-generated electron-hole pairs in the materials. In general, a smaller diameter of the Nyquist plot reflects a lower degree of charge transfer resistance at the electrode-electrolyte interface, which corresponds to a greater degree of charge separation efficiency.<sup>51</sup> Fig. 7a shows the EIS Nyquist plots of the  $\text{ZnIn}_2\text{S}_4/\text{MoS}_2$  composites in comparison with pure  $\text{ZnIn}_2\text{S}_4$ . The  $\text{ZnIn}_2\text{S}_4/\text{MoS}_2$ -40%wt electrode shows the smallest diameter on the EIS Nyquist plot, indicating the lowest level of charge transfer resistance. This implies a significant level of efficiency of the charge separation and interfacial charge transportation between  $\text{ZnIn}_2\text{S}_4$  and  $\text{MoS}_2$  in the  $\text{ZnIn}_2\text{S}_4/\text{MoS}_2$ -40%wt heterostructure. In addition, the EIS Nyquist plot of the  $\text{ZnIn}_2\text{S}_4/\text{MoS}_2$  physical mixture (mixed-40%) is larger than that of  $\text{ZnIn}_2\text{S}_4$  and  $\text{ZnIn}_2\text{S}_4/\text{MoS}_2$ -40%wt, suggesting a poor interfacial interaction between  $\text{ZnIn}_2\text{S}_4$  and  $\text{MoS}_2$  in the  $\text{ZnIn}_2\text{S}_4/\text{MoS}_2$  physical mixture. This finding suggests that

the stronger interfacial interaction between ZnIn<sub>2</sub>S<sub>4</sub> and MoS<sub>2</sub> results in better electrons–holes separation efficiency, which is essential for improving photocatalytic performance. Furthermore, linear sweep voltammograms (Fig. 7b) shows that photocurrent density of the ZnIn<sub>2</sub>S<sub>4</sub>/MoS<sub>2</sub>-40%wt photoelectrode is enhanced compared with the ZnIn<sub>2</sub>S<sub>4</sub> photoelectrode in the entire scanning region, supporting that the charge carriers generation and separation of ZnIn<sub>2</sub>S<sub>4</sub>/MoS<sub>2</sub>-40%wt are more efficient than those of ZnIn<sub>2</sub>S<sub>4</sub>. The transient photocurrent density-time curve of the ZnIn<sub>2</sub>S<sub>4</sub>/MoS<sub>2</sub>-40%wt photoelectrode (Fig. S6) shows reproducible response with the photocurrent density of about 0.37 mA cm<sup>-2</sup>.

The suppression of the charge recombination process in the ZnIn<sub>2</sub>S<sub>4</sub>/MoS<sub>2</sub>-40%wt heterojunction is supported by photoluminescence spectroscopy (PL). Typically, a lower emission intensity of the PL spectrum means a lower recombination rate of photo-generated electron-hole pairs.<sup>52</sup> Fig. 7c demonstrates the PL spectra of the composite samples under an excitation wavelength of 590 nm. All the samples exhibit similar PL spectra centering at about 670 nm. The PL emission spectrum of the ZnIn<sub>2</sub>S<sub>4</sub>/MoS<sub>2</sub>-40%wt composite is lower in intensity in comparison with ZnIn<sub>2</sub>S<sub>4</sub> and the other composites, implying a lower charge recombination rate as mentioned above. Besides, the lifetime ( $\tau$ ) of the photo-generated charge carriers of the composite was investigated by TRPL in comparison with ZnIn<sub>2</sub>S<sub>4</sub>. The TRPL decay spectra are shown in Fig. 7d. The spectra were fitted to a bi-exponential function.<sup>53 54</sup> The fitting parameter and the parameters used for the calculation of the average exciton lifetime are listed in Table S1. The average lifetime for ZnIn<sub>2</sub>S<sub>4</sub>/MoS<sub>2</sub>-40%wt (17.81 ns) is longer than that for ZnIn<sub>2</sub>S<sub>4</sub> (13.77 ns), which is attributed to the more rapid transfer of photo-generated electrons and holes through the interfacial contact in the ZnIn<sub>2</sub>S<sub>4</sub>/MoS<sub>2</sub> heterojunction. Consequently, the recombination of electron–hole pairs is hindered and the number of photo-generated electrons to participate in the reduction reactions is increased.<sup>55 56</sup> The EIS, PL and TRPL results specify that the formation of the ZnIn<sub>2</sub>S<sub>4</sub>/MoS<sub>2</sub> heterojunction with an

appropriate loading amount of MoS<sub>2</sub> can increase the charge separation and transportation efficiencies, and reduce the recombination rate of photogenerated electrons and holes.

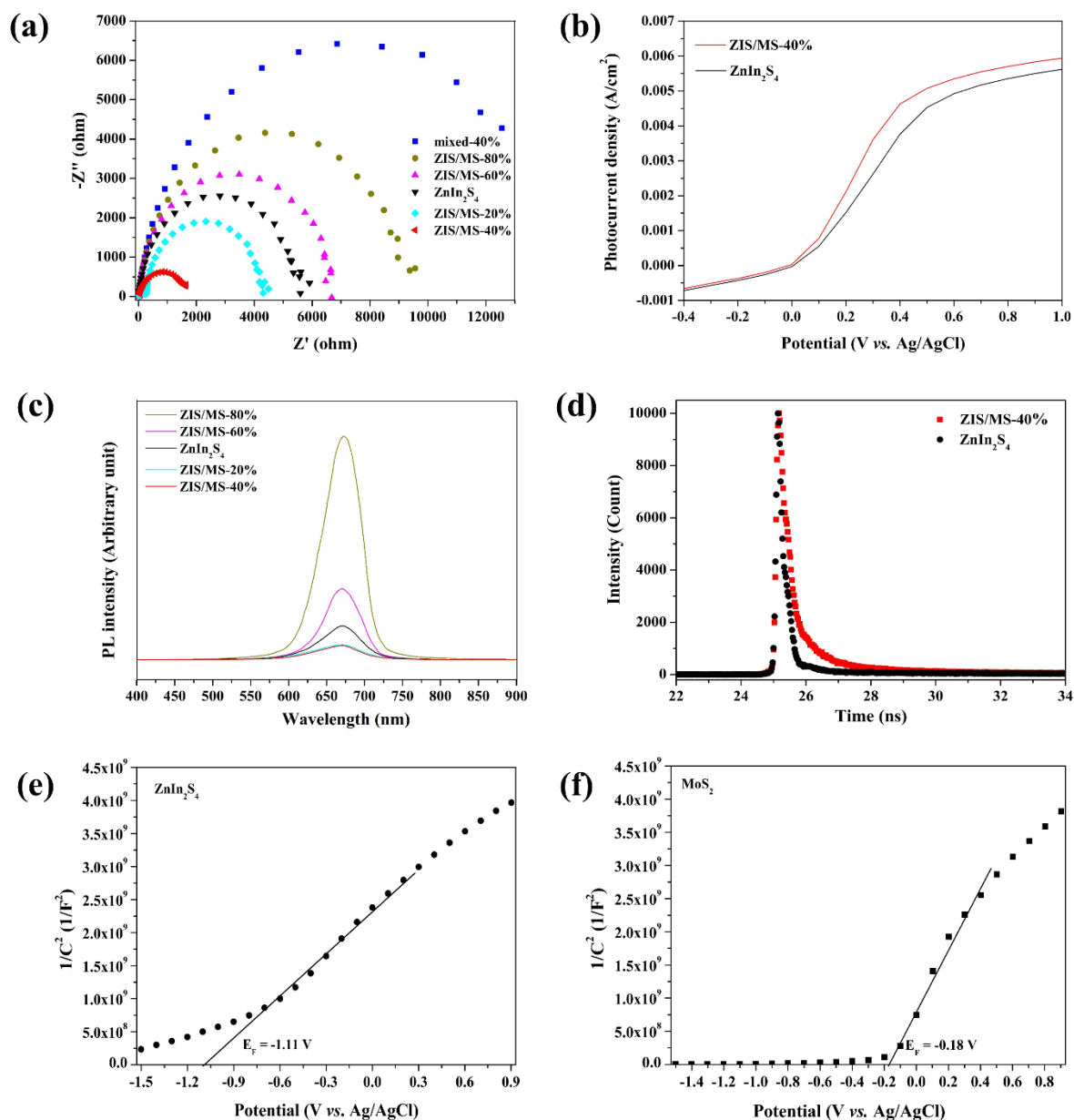


**Fig. 7.** (a) EIS Nyquist plots, (b) linear sweep voltammograms, (c) PL emission spectra and (d) time-resolved photoluminescence decay spectra of ZnIn<sub>2</sub>S<sub>4</sub>/MoS<sub>2</sub> compared with the ZnIn<sub>2</sub>S<sub>4</sub>. Mott-Schottky plots of (e) ZnIn<sub>2</sub>S<sub>4</sub> and (f) MoS<sub>2</sub> electrodes.

The energy band positions of ZnIn<sub>2</sub>S<sub>4</sub> and MoS<sub>2</sub> were calculated according to the Mulliken electronegativity theory by using the following equations:  $E_{CB} = X - E^e - 0.5E_g$  and  $E_{VB} = E_{CB} + E_g$ , where  $E_{VB}$  and  $E_{CB}$  represent the valence and conduction band potentials, respectively.<sup>57 58</sup> Additionally, X is the absolute electronegativity of the semiconductor materials (4.82 eV for ZnIn<sub>2</sub>S<sub>4</sub><sup>57</sup> and 5.36 eV for MoS<sub>2</sub><sup>59</sup>),  $E^e$  is the estimated energy of the free electrons on the hydrogen scale (about 4.5 eV) and  $E_g$  is the band gap energy of the semiconductor materials. According to the calculated  $E_g$  values (2.81 eV for ZnIn<sub>2</sub>S<sub>4</sub> and 1.96 eV for MoS<sub>2</sub>) obtained from the UV-visible DRS analysis, the  $E_{VB}$  and  $E_{CB}$  values of ZnIn<sub>2</sub>S<sub>4</sub> are 1.71 eV and -1.10 eV, respectively, while the  $E_{VB}$  and  $E_{CB}$  values of MoS<sub>2</sub> are 1.84 eV and -0.12 eV, respectively.<sup>60</sup> The  $E_{VB}$  and  $E_{CB}$  of ZnIn<sub>2</sub>S<sub>4</sub> and MoS<sub>2</sub> were also calculated from the Mott-Schottky measurements. As is shown in Figs. 7e and 7f, the positive slope of the linear plots for the ZnIn<sub>2</sub>S<sub>4</sub> and MoS<sub>2</sub> electrodes indicates that ZnIn<sub>2</sub>S<sub>4</sub> and MoS<sub>2</sub> are n-type semiconductors. By extrapolating the linear portion of the Mott–Schottky plots to  $1/C^2 = 0$ , the flat band potentials ( $E_F$ ) of the ZnIn<sub>2</sub>S<sub>4</sub> and MoS<sub>2</sub> electrodes are -1.11 and -0.18 V (vs. Ag/AgCl), which can be converted to -0.90 and 0.03 V (vs. NHE), respectively. Typically,  $E_{CB}$  of an n-type semiconductor is ~0.1 V more negative than its flat band potential. Therefore,  $E_{CB}$  of ZnIn<sub>2</sub>S<sub>4</sub> and MoS<sub>2</sub> are -1.00 and -0.07 V (vs. NHE), respectively. Combining with their  $E_g$  values,  $E_{VB}$  of ZnIn<sub>2</sub>S<sub>4</sub> and MoS<sub>2</sub> are calculated as 1.81 and 1.89 V, respectively. As is summarized in Table S2,  $E_{VB}$  and  $E_{CB}$  of ZnIn<sub>2</sub>S<sub>4</sub> and MoS<sub>2</sub> calculated from the Mott-Schottky measurements are close to the values obtained from the theoretical calculation.

### 3.2.2. Photocatalytic H<sub>2</sub> production activity

Photocatalytic H<sub>2</sub> production activity of the ZnIn<sub>2</sub>S<sub>4</sub>/MoS<sub>2</sub> composites under UV-visible light irradiation were investigated. As is shown in Fig. 8a, ZnIn<sub>2</sub>S<sub>4</sub> and MoS<sub>2</sub> photocatalysts can produce H<sub>2</sub> gas at the production rates of 111.6 and 13.3  $\mu\text{mol h}^{-1} \text{g}^{-1}$ , respectively. After

ZnIn<sub>2</sub>S<sub>4</sub> is introduced by 20, 30 and 40%wt of MoS<sub>2</sub>, these ZnIn<sub>2</sub>S<sub>4</sub>/MoS<sub>2</sub> composites can produce H<sub>2</sub> gas at higher rates at up to 153.3, 163.3 and 200.1 μmol h<sup>-1</sup> g<sup>-1</sup>, respectively. The improved activity of these ZnIn<sub>2</sub>S<sub>4</sub>/MoS<sub>2</sub> composites is originated by enhanced charge separation efficiency and transportation, as well as by charge recombination suppression at the contact interface between ZnIn<sub>2</sub>S<sub>4</sub> and MoS<sub>2</sub> in the ZnIn<sub>2</sub>S<sub>4</sub>/MoS<sub>2</sub> heterojunction. However, the ZnIn<sub>2</sub>S<sub>4</sub>/MoS<sub>2</sub> composites with higher amounts of MoS<sub>2</sub> (50, 60 and 80% wt) decrease the H<sub>2</sub> production rate to 126.6, 96.6 and 66.6 μmol h<sup>-1</sup> g<sup>-1</sup>, respectively. This is probably because the excess MoS<sub>2</sub> particles with less activity could mask the active sites of the ZnIn<sub>2</sub>S<sub>4</sub> surface and could also reduce the light absorption capability of the composites. As a result, the quantity of photogenerated charges and active species involved in the photocatalytic reactions are decreased. Therefore, a suitable amount of MoS<sub>2</sub> in the ZnIn<sub>2</sub>S<sub>4</sub>/MoS<sub>2</sub> composite is necessary for optimizing photocatalytic activity due to the significant synergistic effect between the two single-components for the photocatalytic reactions. Among the other photocatalysts, the ZnIn<sub>2</sub>S<sub>4</sub>/MoS<sub>2</sub> composite with 40%wt of MoS<sub>2</sub> is the most efficient photocatalyst proving a greatly enhanced level of efficacy, where the rate of H<sub>2</sub> reduction by this composite photocatalyst is approximately 1.8 and 15.1 times faster than that of ZnIn<sub>2</sub>S<sub>4</sub> and MoS<sub>2</sub>, respectively. The AQY value of ZnIn<sub>2</sub>S<sub>4</sub>/MoS<sub>2</sub>-40%wt (0.19%) for H<sub>2</sub> reduction reaction is also higher when compared with ZnIn<sub>2</sub>S<sub>4</sub> (0.10%). Furthermore, this composite shows remarkably higher activity (200.1 μmolh<sup>-1</sup>g<sup>-1</sup>) than the physical mixture of ZnIn<sub>2</sub>S<sub>4</sub> and 40%wt of MoS<sub>2</sub> (60.3 μmolh<sup>-1</sup>g<sup>-1</sup>), highlighting a determination that the strong chemical interaction between two single-components in the ZnIn<sub>2</sub>S<sub>4</sub>/MoS<sub>2</sub> heterojunction is necessary for the improvement of photocatalytic activity. The photocatalytic activity of ZnIn<sub>2</sub>S<sub>4</sub>/MoS<sub>2</sub>-40%wt for the H<sub>2</sub> production reaction was also tested under UV-visible and visible light regions using 385 nm and 400 nm cut-off filters, respectively, and the results are shown in Fig 8b. The activity of ZnIn<sub>2</sub>S<sub>4</sub>/MoS<sub>2</sub>-40%wt is still higher than ZnIn<sub>2</sub>S<sub>4</sub> under both UV-visible and visible regions,

confirming that the introduction of MoS<sub>2</sub> to ZnIn<sub>2</sub>S<sub>4</sub> can improve the visible-light absorption ability. The H<sub>2</sub> production rate of the synthesized ZnIn<sub>2</sub>S<sub>4</sub>/MoS<sub>2</sub> photocatalyst in this work compared with the previous literature reports are shown in Table S3. The difference in the H<sub>2</sub> production rate could be caused by the variations in the synthesis method and the photocatalytic conditions such as the power of the light source and type/concentration of sacrificial reagents.

<sup>61 62 63</sup> The detailed discussions on the variations are provided in the Supporting Information.

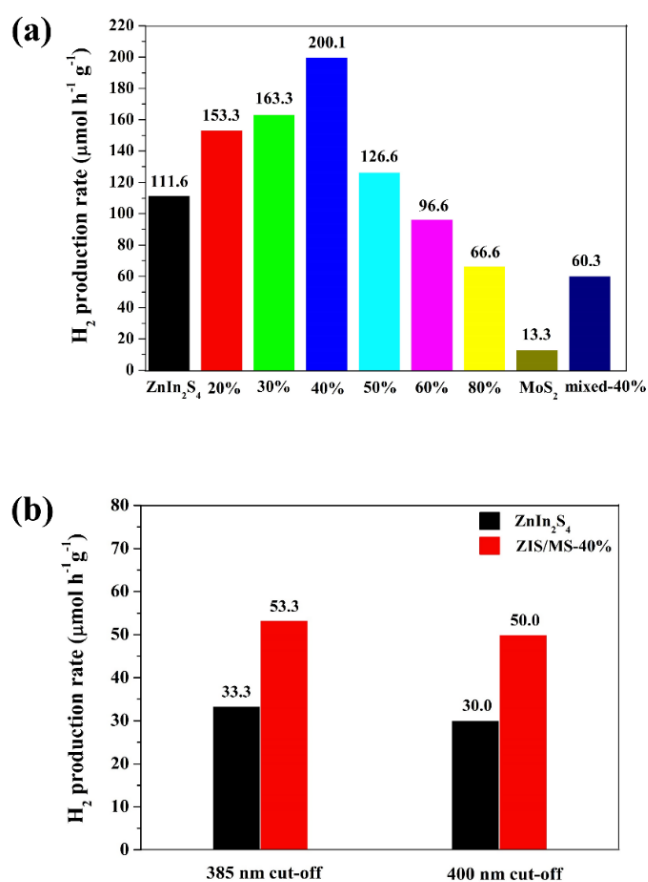


**Fig. 8. (a)** H<sub>2</sub> production rate of the ZnIn<sub>2</sub>S<sub>4</sub>, MoS<sub>2</sub> and ZnIn<sub>2</sub>S<sub>4</sub>/MoS<sub>2</sub> photocatalysts under UV-visible light irradiation. **(b)** H<sub>2</sub> production rate of the ZnIn<sub>2</sub>S<sub>4</sub>/MoS<sub>2</sub>-40% wt photocatalyst under UV-visible and visible light regions in comparison with the ZnIn<sub>2</sub>S<sub>4</sub> photocatalyst.

### 3.2.3. Photocatalytic Cr(VI) reduction activity

The photocatalytic Cr(VI) reduction activities of the ZnIn<sub>2</sub>S<sub>4</sub>/MoS<sub>2</sub>-40%wt, ZnIn<sub>2</sub>S<sub>4</sub> and MoS<sub>2</sub> photocatalysts under visible light irradiation are shown in Fig. 9a. After 120 min of light irradiation, the ZnIn<sub>2</sub>S<sub>4</sub>/MoS<sub>2</sub>-40%wt photocatalyst exhibits the highest degree of photoreduction efficiency (82.8%) when compared with ZnIn<sub>2</sub>S<sub>4</sub> (73.3%) and MoS<sub>2</sub> (11.6%). The kinetics of the photocatalytic Cr(VI) reduction reaction in the presence of these photocatalysts are presented in Fig. 9b. The photoreduction of Cr(VI) follows the pseudo-first-order kinetic model:  $\ln(C_0/C) = kt$ , where  $C_0$  is the initial concentration of Cr(VI),  $C$  is the concentration of Cr(VI) at time  $t$ ,  $t$  is the irradiation time and  $k$  is the kinetic rate constant ( $\text{min}^{-1}$ ). The  $k$  value of ZnIn<sub>2</sub>S<sub>4</sub>/MoS<sub>2</sub>-40%wt, determined from the slope of the line, is  $1.4 \times 10^{-2} \text{ min}^{-1}$  which is 1.3 and 17.5 times higher than that of ZnIn<sub>2</sub>S<sub>4</sub> ( $1.1 \times 10^{-2} \text{ min}^{-1}$ ) and MoS<sub>2</sub> ( $0.8 \times 10^{-3} \text{ min}^{-1}$ ), respectively. Moreover, the photoreduction efficiency of ZnIn<sub>2</sub>S<sub>4</sub>/MoS<sub>2</sub>-40%wt is 1.7 times higher than that of the physical mixture (47.5% with a  $k$  value of  $4.8 \times 10^{-3} \text{ min}^{-1}$ ). Furthermore, the AQY value of ZnIn<sub>2</sub>S<sub>4</sub>/MoS<sub>2</sub>-40%wt (0.91%) for Cr(VI) reduction reaction is about 1.2 times higher than that of ZnIn<sub>2</sub>S (0.76%). These findings demonstrate that MoS<sub>2</sub> is an effective co-catalyst for improving the photocatalytic efficiency of the ZnIn<sub>2</sub>S<sub>4</sub> photocatalyst. It should be noted that, in the blank experiment, the concentration of Cr(VI) is unchanged. This result clearly suggests that the presence of the photocatalyst is needed to achieve the Cr(VI) photoreduction and that the Cr(VI) ion would be stable during the photolytic reaction.

The effect of pH of the solution on the photoreduction efficiency of the ZnIn<sub>2</sub>S<sub>4</sub>/MoS<sub>2</sub>-40%wt photocatalyst was also investigated under constant photocatalyst dosage and initial Cr(VI) concentration. As is presented in Figs. 9c-9d, greater efficiency was obtained when the experiments were carried out in acidic solutions than when in alkaline solution; 95.3%, 82.8% and 59.2% of the photoreduction efficiency with  $k$  values of  $1.4 \times 10^{-2}$ ,  $2.3 \times 10^{-2}$  and  $6.6 \times 10^{-3}$

$\text{min}^{-1}$  achieve at pH values of 4, 6 (initial pH) and 8, respectively. The efficiency of the composite photocatalyst decreases markedly with an increase in the pH of the solution. This result is related to the different forms of the oxidation state Cr(VI) in the different pH values of the solutions. Under acidic conditions, dichromate ( $\text{Cr}_2\text{O}_7^{2-}$ ) and hydrogenchromate ( $\text{HCrO}_4^-$ ) are the dominant forms of Cr(VI) species, while chromate ( $\text{CrO}_4^{2-}$ ) is the dominant species under basic condition.<sup>28</sup> Additionally, it is easier to reduce  $\text{Cr}_2\text{O}_7^{2-}$  and  $\text{HCrO}_4^-$  ions by photo-generated electrons since the reduction potentials of  $\text{Cr}_2\text{O}_7^{2-}/\text{Cr}^{3+}$  (1.33 V vs. NHE) and  $\text{HCrO}_4^-/\text{Cr}^{3+}$  (1.35 V vs. NHE) are more positive than that of  $\text{CrO}_4^{2-}/\text{Cr}(\text{OH})_3$  (-0.13 V vs. NHE).<sup>64</sup> Furthermore, the surface of the photocatalyst may be protonated under acidic conditions, which simplifies the negatively Cr(VI) species to be adsorbed.<sup>65</sup> In addition, under alkaline conditions, the precipitated  $\text{Cr}(\text{OH})_3$  that occurs in the system is deposited on the surface of the photocatalyst resulting in the decrease in photoreduction efficiency.<sup>66</sup>

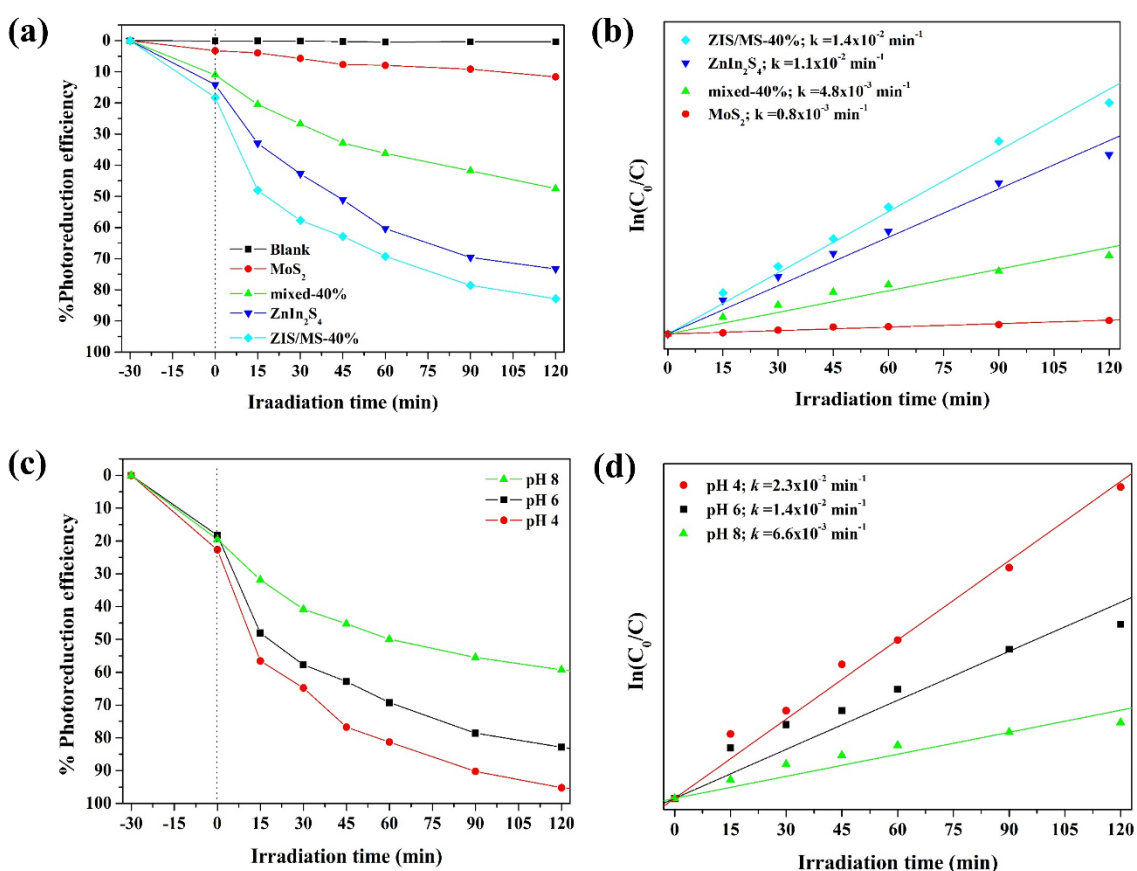


**Fig. 9.** (a) Photoreduction efficiency and (b) pseudo-first-order kinetic plots of the Cr(VI) photoreduction at pH 6 (initial pH) in the presence of ZnIn<sub>2</sub>S<sub>4</sub>/MoS<sub>2</sub>-40%wt in comparison with ZnIn<sub>2</sub>S<sub>4</sub>, MoS<sub>2</sub> and physical mixture of MoS<sub>2</sub> (40%wt) and ZnIn<sub>2</sub>S<sub>4</sub>. (c) Effect of pH of the solution and (d) pseudo-first-order kinetic plots of the Cr(VI) photoreduction in the presence of ZnIn<sub>2</sub>S<sub>4</sub>/MoS<sub>2</sub>-40% wt.

#### 3.2.4. Photocatalytic mechanisms for the H<sub>2</sub> production and Cr(VI) reduction reactions

As a consequence of the matched overlapping band structures of ZnIn<sub>2</sub>S<sub>4</sub> and MoS<sub>2</sub> and the results from the photocatalytic reduction tests, either conventional type-II heterojunction (Fig. S7a) or Z-scheme heterojunction (Fig. S7b) could be formed.<sup>15 67</sup> To investigate the charge transfer pathway in the ZnIn<sub>2</sub>S<sub>4</sub>/MoS<sub>2</sub> heterostructure, a silver (Ag) photo-deposition experiment was carried out and the depositing of Ag on the composite was investigated by TEM. The procedures of this experiment are provided in the Supporting Information. The high-magnified TEM images (Fig. S8) show that the MoS<sub>2</sub> particle was deposited by Ag nanoparticle with a lattice fringe of 0.24 nm, which corresponds to the (111) plane of Ag. This result indicates that the reduction of Ag<sup>+</sup> ion by light irradiation occurs on MoS<sub>2</sub>, implying that photo-generated electrons accumulate on the surface of MoS<sub>2</sub> rather than on the surface of ZnIn<sub>2</sub>S<sub>4</sub>. Based on this result and the band positions of these two components, the photo-generated carrier transport mechanism occur through the type-II heterojunction between ZnIn<sub>2</sub>S<sub>4</sub> and MoS<sub>2</sub>, in which electrons from CB of ZnIn<sub>2</sub>S<sub>4</sub> migrate to CB of MoS<sub>2</sub>. This outcome is consistent with the findings of previous reports.<sup>21, 23</sup>

A photocatalytic mechanism for the enhanced H<sub>2</sub> production rate of the ZnIn<sub>2</sub>S<sub>4</sub>/MoS<sub>2</sub> photocatalyst is presented in Fig. 10a. After ZnIn<sub>2</sub>S<sub>4</sub>/MoS<sub>2</sub> is exposed to visible light radiation, the photo-generated electrons and holes are generated from the ZnIn<sub>2</sub>S<sub>4</sub> and MoS<sub>2</sub> components in the composite photocatalyst (Eq. 1). The photo-generated electrons are then transferred to

their conduction bands ( $C_B$ ), leaving holes in their valence bands ( $V_B$ ). After that, the electrons can be transferred from  $C_B$  of  $ZnIn_2S_4$  to  $C_B$  of  $MoS_2$  since the conduction band potential ( $E_{CB}$ ) of  $ZnIn_2S_4$  (-1.00 V) is more negative than that of  $MoS_2$  (-0.07 V). Meanwhile, the holes are also transferred from  $V_B$  of  $MoS_2$  to the  $V_B$  of  $ZnIn_2S_4$  because of the less positive valence band potential ( $E_{VB}$ ) of  $ZnIn_2S_4$  (1.81 V). The accumulated electrons on  $C_B$  of  $MoS_2$  can reduce  $H^+$  to generate  $H_2$  (Eq. 2) due to the more negative potential of its CB (-0.07 V) than the hydrogen reduction potential ( $H^+/H_2 = 0.00$  V vs. NHE). Moreover, the adsorbed  $H^+$  ions on the exposed sulfur edges of  $MoS_2$  are easily reduced to  $H_2$  by the photo-generated electrons.<sup>68</sup> Simultaneously, the holes in  $V_B$  of  $ZnIn_2S_4$  are consumed by the sacrificial reagents (Eq. 3) to generate oxidation products, substantially enhancing the photocatalytic  $H_2$  production activity.<sup>69</sup> Therefore, this coupled system is favorable for the separation and migration of photo-generated charge carriers through the  $ZnIn_2S_4/MoS_2$  heterojunction at the interfacial interaction, which is a key factor in determining the photocatalytic  $H_2$  production activity. The step-wise photocatalytic  $H_2$  production mechanisms are provided as follows:



A photocatalytic mechanism for the enhanced Cr(VI) reduction efficiency of the  $ZnIn_2S_4/MoS_2$ -40%wt composite is proposed in Fig. 10b. When the  $ZnIn_2S_4/MoS_2$ -40%wt composite is excited by visible light radiation, both  $ZnIn_2S_4$  and  $MoS_2$  components in the composite produce photo-generated electrons and holes (Eq. 1). The holes from  $V_B$  of  $MoS_2$  can migrate to the  $V_B$  of  $ZnIn_2S_4$ , and oxidize  $H_2O$  to yield  $O_2$  (Eq. 4) owing to the less positive potential of  $O_2/H_2O$  (1.23 V vs. NHE) than the potential of  $V_B$  of  $ZnIn_2S_4$  (1.81 V).<sup>70</sup> At the

same time, the electrons from  $C_B$  of  $ZnIn_2S_4$  can rapidly be transferred to  $C_B$  of  $MoS_2$ , and then react with the  $Cr(VI)$  ion to  $Cr(III)$  ion (Eq. 5-7) owing to the more negative potential of  $C_B$  of  $MoS_2$  (-0.07 V) than the potential of  $Cr(VI)/Cr(III)$ .<sup>64</sup> The step-wise photocatalytic  $Cr(VI)$  reduction mechanisms are provided as follows:



under acidic conditions,



under basic condition,

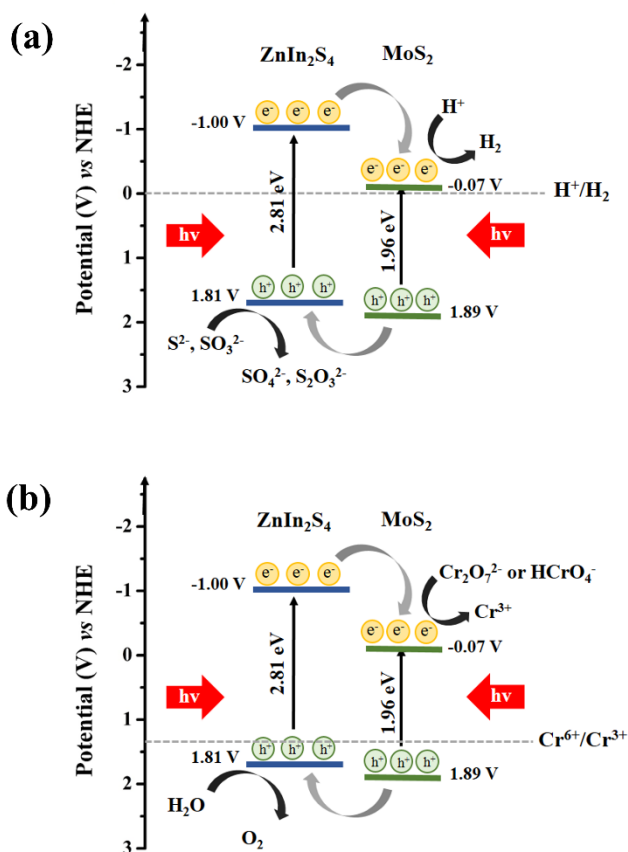


**Fig. 10.** Schematic illustrations of the proposed mechanisms of the ZnIn<sub>2</sub>S<sub>4</sub>/MoS<sub>2</sub> photocatalyst for (a) H<sub>2</sub> production and (b) Cr(VI) reduction reactions under visible light irradiation.

### 3.2.5. Reusability and photocatalytic stability

The recycling of the experiments of the ZnIn<sub>2</sub>S<sub>4</sub>/MoS<sub>2</sub>-40%wt photocatalyst were carried out for photocatalytic H<sub>2</sub> production and Cr(VI) reduction reactions under the same conditions to evaluate its photocatalytic stability. Fig. 11a shows the H<sub>2</sub> production rate of the ZnIn<sub>2</sub>S<sub>4</sub>/MoS<sub>2</sub>-40%wt photocatalyst in comparison with ZnIn<sub>2</sub>S<sub>4</sub>. After three-cycles of use, the H<sub>2</sub> production rate for the ZnIn<sub>2</sub>S<sub>4</sub> photocatalyst is dramatically decreased. The ZnIn<sub>2</sub>S<sub>4</sub> photocatalyst provides H<sub>2</sub> production rate of 111.6, 67.3 and 39.2 μmol h<sup>-1</sup> g<sup>-1</sup>, while the ZnIn<sub>2</sub>S<sub>4</sub>/MoS<sub>2</sub>-40%wt photocatalyst provides H<sub>2</sub> production rate of 200.1, 198.3 and 196.6 μmol h<sup>-1</sup> g<sup>-1</sup> in the first, second and third runs, respectively. When compared with ZnIn<sub>2</sub>S<sub>4</sub>, the efficiency of ZnIn<sub>2</sub>S<sub>4</sub>/MoS<sub>2</sub>-40%wt photocatalyst shows insignificant losses after three cycle uses. The reusability of the ZnIn<sub>2</sub>S<sub>4</sub>/MoS<sub>2</sub>-40%wt photocatalyst for the H<sub>2</sub> production reaction is found to be 98.3% after three cycle uses. A slight decrease in the reusability of the ZnIn<sub>2</sub>S<sub>4</sub>/MoS<sub>2</sub>-40%wt photocatalyst could be due to the loss of the photocatalyst amount during the recovery procedure. The recovered weight of the ZnIn<sub>2</sub>S<sub>4</sub>/MoS<sub>2</sub>-40%wt photocatalyst decreased from 0.100 to 0.942 and 0.895 mg from the first, second and third runs, respectively. Additionally, the recycling experiments for the Cr(VI) photoreduction in a pH solution of 4 was also performed to evaluate the stability of the ZnIn<sub>2</sub>S<sub>4</sub>/MoS<sub>2</sub>-40%wt photocatalyst in a strong acidic environment. As is presented in Fig. 11b, the photoreduction efficiency slightly decrease from 95.3% to 93.1% and 92.8% in the first, second and third runs, respectively. The efficiency of the ZnIn<sub>2</sub>S<sub>4</sub>/MoS<sub>2</sub>-40%wt photocatalyst remains at high levels after the third cycle. The used ZnIn<sub>2</sub>S<sub>4</sub>/MoS<sub>2</sub>-40%wt photocatalyst after the three-run

photocatalytic H<sub>2</sub> production and Cr(VI) reduction reactions was collected and analyzed by SEM and XRD. The SEM images of the used photocatalyst for both reactions (Figs. 11c-11d) reveal that the morphology is retained after the three-cycling test. In addition, the XRD patterns (Fig. 11e) of this used photocatalyst are similar to the fresh photocatalyst without the addition of impurity peaks. These results demonstrate that the ZnIn<sub>2</sub>S<sub>4</sub>/MoS<sub>2</sub>-40%wt photocatalyst possesses good reusability and stability with effective photocatalytic activity for H<sub>2</sub> production and Cr(VI) reduction reactions. These outcomes could be that the intimate contact between ZnIn<sub>2</sub>S<sub>4</sub> and MoS<sub>2</sub> particles in the composite favors the vectorial transfer of photo-generated electrons from CB of ZnIn<sub>2</sub>S<sub>4</sub> to MoS<sub>2</sub>, which is beneficial for preventing the reduction of Zn<sup>2+</sup> and In<sup>3+</sup> ions in the composite. <sup>12 71</sup>

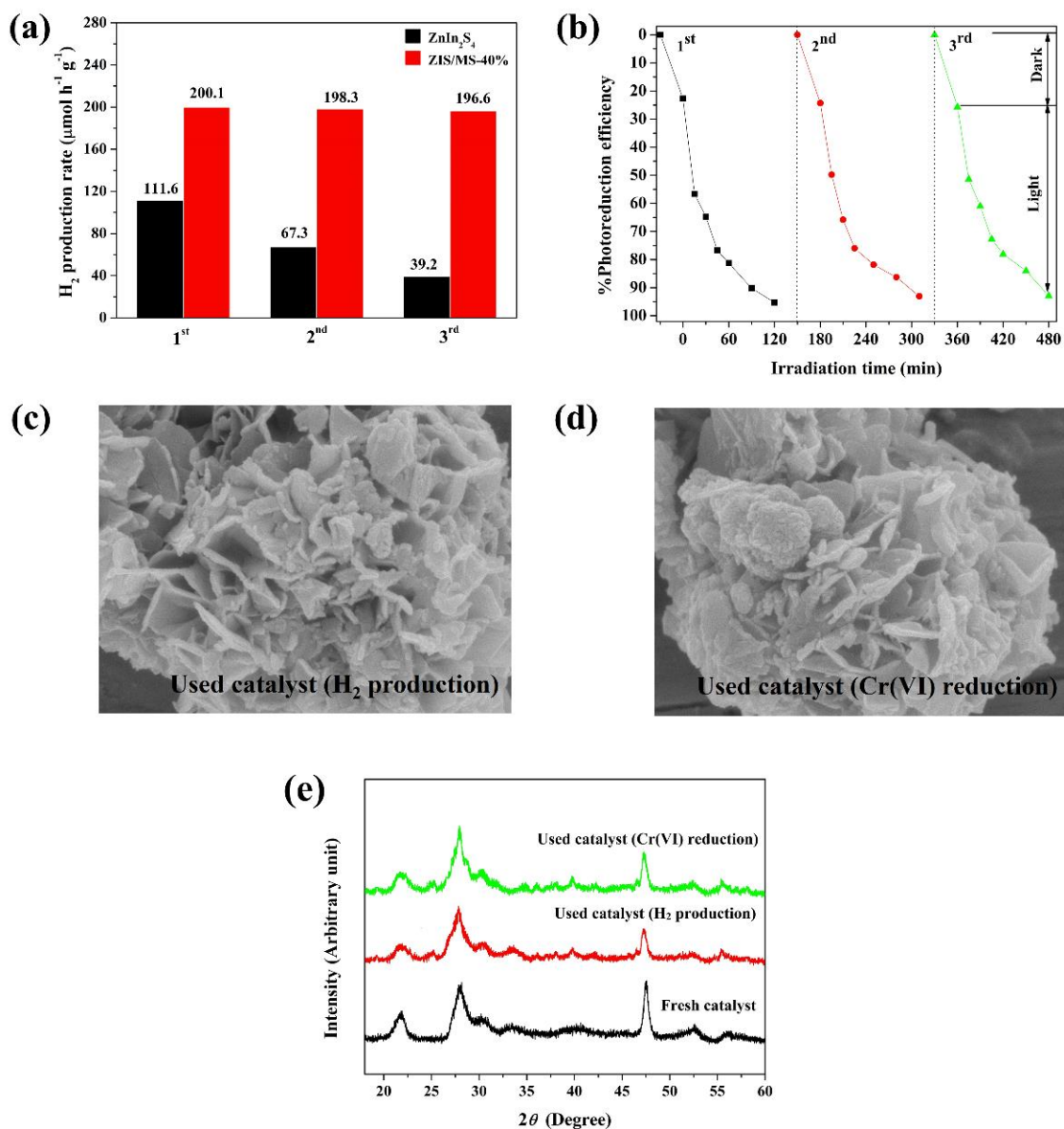


**Fig. 11.** Recycling experiments of the ZnIn<sub>2</sub>S<sub>4</sub>/MoS<sub>2</sub>-40%wt photocatalyst **(a)** for photocatalytic H<sub>2</sub> production in comparison with ZnIn<sub>2</sub>S<sub>4</sub> **(b)** for the Cr(VI) photoreduction under pH solution of 4. **(c-d)** SEM images and **(e)** XRD patterns of the fresh and used ZnIn<sub>2</sub>S<sub>4</sub>/MoS<sub>2</sub>-40%wt photocatalysts after the third run.

#### 4. Conclusions

The flower-like ZnIn<sub>2</sub>S<sub>4</sub> microspheres with multi-cavities and the series of ZnIn<sub>2</sub>S<sub>4</sub>/MoS<sub>2</sub> photocatalysts were successfully synthesized using the biomolecule-assisted microwave

heating method. The loading amount of MoS<sub>2</sub> played an important role on photocatalytic H<sub>2</sub> production under UV-visible light irradiation. Among all the fabricated ZnIn<sub>2</sub>S<sub>4</sub>/MoS<sub>2</sub> photocatalysts, ZnIn<sub>2</sub>S<sub>4</sub>/MoS<sub>2</sub>-40% wt provided the highest level of photocatalytic activity for H<sub>2</sub> production and was higher than ZnIn<sub>2</sub>S<sub>4</sub> under UV-visible and visible regions; 200.1 and 50.0 μmol h<sup>-1</sup> g<sup>-1</sup> under UV-visible and visible light irradiation, respectively. In addition, this photocatalyst also displayed the greatest photocatalytic activity for Cr(VI) reduction under visible light irradiation. The Cr(VI) solution at pH 4 was reduced by up to 95.3% within 120 min. Moreover, the ZnIn<sub>2</sub>S<sub>4</sub>/MoS<sub>2</sub>-40% wt photocatalyst also displayed good stability and recycling performance after three tests. The enhanced photocatalytic performance and photostability of ZnIn<sub>2</sub>S<sub>4</sub>/MoS<sub>2</sub>-40% wt were attributed to the increase in visible-light response and efficient separation and migration of photo-generated charge carriers derived by the formation of the type-II heterojunction structure between ZnIn<sub>2</sub>S<sub>4</sub> and MoS<sub>2</sub>. Notably, this ZnIn<sub>2</sub>S<sub>4</sub>/MoS<sub>2</sub> heterojunction is a potential efficient visible-light-responsive photocatalyst for water splitting and for the removal of heavy metals in industrial wastewater.

## Acknowledgments

This research work was partially supported by Chiang Mai University and the Center of Excellence for Innovation in Chemistry (PERCH-CIC), Ministry of Higher Education, Science, Research and Innovation, Faculty of Science, Chiang Mai University. The authors would like to acknowledge the Science Achievement Scholarship of Thailand for financial support towards Watcharapong Pudkon. We also thank Dr. Filip Kielar from Naresuan University for the operation of the time-resolved photoluminescence measurement.

## References

1. A. Kudo and Y. Miseki, *Chem. Soc. Rev.*, 2009, **38**, 253-278

2. M. R. Hoffmann, S. T. Martin, W. Choi and D. W. Bahnemann, *Chem. Rev.s*, 1995, **95**, 69-96.
3. M. Ge, J. Cai, J. Iocozzia, C. Cao, J. Huang, X. Zhang, J. Shen, S. Wang, S. Zhang, K. Q. Zhang, Y. Lai and Z. Lin, *Int. J. Hydrogen Energy*, 2016, **42**, 8418-8449 .
4. Q. Li, C. Cui, H. Meng and J. Yu, *Chem. Asian J.*, 2014, **9**, 1766-1770.
5. Z. Lei, W. You, M. Liu, G. Zhou, T. Takata, M. Hara, K. Domen and C. Li, *Chem. Commun.*, 2003, **17**, 2142-2143.
6. G. Zhang, D. Chen, N. Li, Q. Xu, H. Li, J. He and J. Lu, *Appl. Catal. B*, 2018, **232**, 164-174.
7. L. Wei, Y. Chen, Y. Lin, H. Wu, R. Yuan and Z. Li, *Appl. Catal. B*, 2014, **144**, 521-527.
8. X. L. Gou, F. Y. Cheng, Y. H. Shi, L. Zhang, S. J. Peng, J. Chen and P. W. Shen, *J. Am. Chem. Soc.*, 2006, **128**, 7222-7229.
9. S. Shen, L. Zhao and L. Guo, *Int. J. Hydrogen Energy*, 2008, **33**, 4501-4510.
10. F. Tian, R. Zhu, K. Song, F. Ouyang and G. Cao, *Int. J. Hydrogen Energy*, 2015, **40**, 2141-2148.
11. K. Song, R. Zhu, F. Tian, G. Cao and F. Ouyang, *J. Solid State Chem.*, 2015, **232**, 138-143.
12. Y. Chen, G. Tian, Z. Ren, K. Pan, Y. Shi, J. Wang and H. Fu, *ACS Appl. Mater. Interfaces*, 2014, **6**, 13841-13849.
13. Z. Chen, Y. Wu, J. Xu, F. Wang, J. Wang, J. Zhang, Z. Ren, Y. He and G. Xiao, *J. Mol. Catal. A Chem.*, 2015, **401**, 66-72.
14. W. J. Fan, Z. F. Zhou, W. B. Xu, Z. F. Shi, F. M. Ren, H. H. Ma and S. W. Huang, *Int. J. Hydrogen Energy*, 2010, **35**, 6525-6530.
15. J. Low, J. Yu, M. Jaroniec, S. Wageh and A. Al-Ghamdi, *Adv. Mater.*, 2017, **29**, 160194(1)-160194(12).
16. W. Cui, D. Guo, L. Liu, J. Hu, D. Rana and Y. Liang, *Catal. Commun.*, 2014, **48**, 55-59.
17. D. Sudha and P. Sivakumar, *Chem. Eng. Process.*, 2015, **97**, 112-133.
18. D. Merki and X. Hu, *Energy Environ. Sci.*, 2011, **4**, 3878-3888.
19. J. Mao, Y. Wang, Z. Zheng and D. Deng, *Front. Phys.* 2018, **13**, 138118.
20. S. K. Park, S. H. Yu, S. Woo, J. Ha, J. Shin, Y. E. Sung and Y. Piao, *Cryst. Eng. Comm.*, 2012, **14**, 8323-8325.
21. Z. Zhang, L. Huang, J. Zhang, F. Wang, Y. Xie, X. Shang, Y. Gu, H. Zhao and X. Wang, *Appl. Catal. B*, 2018, **233**, 112-119.

22. C. Liu, B. Chai, C. Wang, J. Yan and Z. Ren, *Int. J. Hydrogen Energy*, 2018, **43**, 6977-6986.
23. T. Huang, W. Chen, T. Y. Liu, Q. L. Hao and X. H. Liu, *Powder Technol.*, 2017, **315**, 157-162.
24. B. Chai, C. Liu, C. Wang, J. Yan and Z. Ren, *Chinese J. Catal.*, 2017, **38**, 2067-2075.
25. G. Chen, N. Ding, F. Li, Y. Fan, Y. Luo, D. Li and Q. Meng, *Appl. Catal. B*, 2014, **160-161**, 614-620.
26. S. Das, A. K. Mukhopadhyay, S. Datta and D. Basu, *Bull. Mater. Sci.*, 2009, **32**, 1-13.
27. I. Bilecka and M. Niederberger, *Nanoscale*, 2010, **2**, 1358-1374.
28. W. Pudkon, S. Kaowphong, S. Pattison, P. J. Miedziak, H. Bahruji, T. E. Davies, D. J. Morgan and G. J. Hutchings, *Catal. Sci. Technol.*, 2019, **9**, 5698-5711.
29. N. Chumha, T. Thongtem, S. Thongtem, S. Kittiwachana and S. Kaowphong, *Appl. Surf. Sci.*, 2018, **447**, 292-299.
30. S. Kaowphong, P. Dumrongrojthanath, S. Kittiwachana, S. Thongtem and T. Thongtem, *Mater. Lett.*, 2013, **107**, 295-298.
31. W. Jiang, X. Yin, F. Xin, Y. Bi, Y. Liu and X. Li, *Appl. Surf. Sci.*, 2014, **288**, 138-142.
32. C. Siva, C. N. Iswarya, P. Baraneedharan and M. Sivakumar, *Mater. Lett.*, 2014, **134**, 56-59.
33. S. K. Park, S. H. Yu, S. Woo, B. Quan, D. C. Lee, M. K. Kim, Y. E. Sung and Y. Piao, *Dalton Trans.*, 2013, **42**, 2399-2405.
34. S. Chen, S. Li, L. Xiong and G. Wang, *Nano*, 2018, **13**, 1850079(1)-1850079(11).
35. B. J. Islam, M. Furukawa, I. Tateishi, H. Katsumata and S. Kaneco, *Chem. Eng.*, 2019, **3**, 33(1)-33(10).
36. Z. Chen, D. Li, G. Xiao, Y. He and Y. J. Xu, *J. Solid State Chem.*, 2012, **186**, 247-254.
37. F. Tian, R. Zhu, K. Song, M. Niu, F. Ouyang and G. Cao, *Mater. Res. Bull.*, 2015, **70**, 645-650.
38. M. Salavati-Niasari, M. Ranjbar and M. Sabet, *J. Inorg. Organomet. Polymer.*, 2013, **23**, 452-457.
39. Z. Chen, D. Li, W. Zhang, Y. Shao, T. Chen, M. Sun and X. Fu, *J. Phys. Chem.*, 2009, **113**, 4433-4440.
40. Z. B. Alfassi, *Instrument Multi-Element Chemical Analysis*, Springer Science+Business Media, 1998.
41. J. C. R. a. S. Myhra, *Handbook of Surface and Interface Analysis Methods for Problem-Solving*, Talor&Francis Group, 2009.

42. M. Tabata, K. Maeda, T. Ishihara, T. Minegishi, T. Takata and K. Domen, *J. Phys. Chem.*, 2010, **114**, 11215-11220.
43. S. Adhikari, A. V. Charanpahari and G. Madras, *ACS Omega*, 2017, **2**, 6926-6938.
44. M. Gao, L. Zhu, W. L. Ong, J. Wang and G. W. Ho, *Catal. Sci. Technol.*, 2015, **5**, 4703-4726.
45. D. Crandles and E. Fortin, *J. Phys. D*, 1986, **19**, 1751-1758 .
46. H. Lin, X. Chen, H. Li, M. Yang and Y. Qi, *Mater. Lett.*, 2010, **64**, 1748-1750.
47. M. Yi and C. Zhang, *RSC Adv.*, 2018, **8**, 9564-9573.
48. X. Zhang, H. Xu, J. Wang, X. Ye, W. Lei, M. Xue, H. Tang and C. Li, *Nanoscale Res. Lett.*, 2016, **11**, 442(1)-442(9).
49. X. Zhang, X. Huang, M. Xue, X. Ye, W. Lei, H. Tang and C. Li, *Mater.Lett.*, 2015, **148**, 67-70.
50. M. Sun, X. Zhao, Q. Zeng, T. Yan, P. Ji, T. Wu, D. Wei and B. Du, *Appl. Surf. Sci.*, 2017, **407**, 328-336.
51. C. Li, H. Wang, J. Ming, M. Liu and P. Fang, *Int. J. Hydrogen Energy*, 2017, **42**, 16968-16978.
52. Y. Yang, J. Chen, Z. Mao, N. An, D. Wang and B. D. Fahlman, *RSC Adv.*, 2017, **7**, 2333-2341.
53. C. Du, B. Yan, Z. Lin and G. Yang, *J. Mater. Chem. A*, 2020, **8**, 207-217.
54. S. Manchala, V. S. R. K. Tandava, L. R. Nagappagari, S. Muthukonda Venkatakrishnan, D. Jampaiah, Y. M. Sabri, S. K. Bhargava and V. Shanker, *Photoch. Photobio. Sci.*, 2019, **18**, 2952-2964.
55. M. Kombo, L. B. Ma, Y. N. Liu, X. X. Fang, N. Ullah, A. H. Odda and A. W. Xu, *Catal. Sci. Technol.*, 2019, **9**, 2196-2202.
56. Y. Li, Z. Jin, L. Zhang and K. Fan, *Chinese J. Catal.*, 2019, **40**, 390-402.
57. A. Chachvalvutikul, W. Pudkon, T. Luangwanta, T. Thongtem, S. Thongtem, S. Kittiwachana and S. Kaowphong, *Mater. Res. Bull.*, 2019, **111**, 53-60.
58. J. Yu, L. Qi and M. Jaroniec, *J. Phys. Chem. C*, 2010, **114**, 13118-13125.
59. S. A. Ansari and M. H. Cho, *Sci. Rep.*, 2017, **7**, 43055(1)-43055(11).
60. X. Zong, H. Yan, G. Wu, G. Ma, F. Wen, L. Wang and C. Li, *J. Am. Chem. Soc.*, 2008, **130**, 7176-7177.
61. V. Kumaravel, D. M. Imam, A. Badreldin, K. R. Chava, Y. J. Do, M. Kang and A. Abdel-Wahab, *Catalysts*, 2019, **9**, 276(1)-276(35).
62. B. Weng, M. Y. Qi, C. Han, Z. R. Tang and Y. J. Xu, *ACS Catal.*, 2019, **9**, 4642-4687.

63. D. Zhang, J. Cheng, F. Shi, Z. Cheng, X. Yang and M. Cao, *RSC Adv.*, 2015, **5**, 33001-33007.
64. R. P. a. J. J. A. J. Bard, *Standard Potentials in Aqueous Solutions*, Marcel Dekker, New York, 1985.
65. S. Patnaik, G. Swain and K. M. Parida, *Nanoscale*, 2018, **10**, 5950-5964.
66. Q. Wu, J. Zhao, G. Qin, C. Wang, X. Tong and S. Xue, *Appl. Catal. B*, 2013, **142-143**, 142-148.
67. X. Li, H. Hu, L. Xu, C. Cui, D. Qian, S. Li, W. Zhu, P. Wang, P. Lin, J. Pan and C. Li, *Appl. Surf. Sci.*, 2018, **441**, 61-68.
68. K. D. Rasamani, F. Alimohammadi and Y. Sun, *Appl. Mater. Today*, 2017, **20**, 83-91.
69. Y. J. Yuan, Z. J. Ye, H. W. Lu, B. Hu, Y. H. Li, D. Q. Chen, J. S. Zhong, Z. T. Yu and Z. G. Zou, *ACS Catal.*, 2016, **6**, 532-541.
70. S. Nezar, Y. Cherifi, A. Barras, A. Addad, E. Dogheche, N. Saoula, N. A. Laoufi, P. Roussel, S. Szunerits and R. Boukherroub, *Arab. J. Chem.*, 2019, **12**, 215-224.
71. Q. Tian, W. Wu, J. Liu, Z. Wu, W. Yao, J. Ding and C. Jiang, *Dalton Trans.*, 2017, **46**, 2770-2777.